Master's thesis

NTNU
Norwegian University of Science and Technology
Faculty of Engineering
Department of Energy and Process Engineering

Silvia Athisayamohan

Measuring the Cooling Capability of Lithium-Ion Batteries

Master's thesis in Mechanical Engineering
Supervisor: Jacob Joseph Lamb
Co-supervisor: Markus Solberg Wahl
June 2023

NTNU
Norwegian University of
Science and Technology

Silvia Athisayamohan

Measuring the Cooling Capability of Lithium-Ion Batteries

Master's thesis in Mechanical Engineering
Supervisor: Jacob Joseph Lamb
Co-supervisor: Markus Solberg Wahl
June 2023

Norwegian University of Science and Technology
Faculty of Engineering
Department of Energy and Process Engineering

NTNU

Norwegian University of
Science and Technology

Abstract

This thesis aims to measure the cooling capability of Lithium-ion batteries (LiBs). The temperature has been shown to have a significant impact on the longevity of the batteries. A proper cooling system and an optimized design of the thermal management system (TMS) are essential to ensure that the operating temperature is within a safe range during cycling. This prevents overheating and reduces the risk of fire and explosion.

The study investigates the cooling potential of LiBs by examining different cooling setups at various frequencies and their impact on heat dissipation. This is explored by evaluating the thermal conductivity of the electrodes, analyzing Scanning Electron Microscope (SEM) images, and measuring the Cell Cooling Coefficient (CCC). Results from the CCC method indicate that an increase in the frequency range from 0.25Hz to 1Hz does not affect the $CCC_{Surface}$ and remains approximately 0.8W/K for both cases. Furthermore, thermal conductivity measurements gave detailed information on heat transport in the battery. Noticeable variations were observed in the thermal conductivity for dry and wet electrodes under different compaction pressure. SEM images confirm that the battery functioned normally during the CCC measurements and gives an understanding of the thermal properties and electrochemical reactions that occurs in the battery.

The findings of this thesis contribute to the understanding of the thermal properties and thermal management requirements of LiBs. This is a foundation for further research and investigation in cooling systems, which are required to meet the increasing demand for LiBs.

Sammendrag

Denne oppgaven har som formål å evaluere kjøleevnen til litium-ionbatterier. Temperatur har vist seg å ha en betydelig innvirkning på levetiden til batteriene. Et hensiktmessig kjølesystem og en optimalisert utforming av det termiske styringssystemet er avgjørende for å sikre en trygg driftstemperatur under sykluser. Dette forhindrer overoppheting og reduserer risikoen for brann og eksplosjon.

Oppgaven undersøker kjøleevnen til litium-ionbatterier ved å evaluere den termiske ledningsevnen til elektrodene, måle Cell Cooling Coefficient (CCC), og analysere Skanningelektronmikroskop (SEM) bilder. Videre gir målinger av termisk ledningsevne detaljert informasjon om varmetransporten i batteriet. Det ble observert betydelige variasjoner i den termiske ledningsevnen for tørre og våte elektroder under ulike komprimeringstrykk. Resultater fra CCC-metoden indikerer at økning av frekvensområdet 0.25Hz til 1Hz ikke påvirker $CCC_{Surface}$, som forblir omtrent 0.8W/K i begge tilfeller. SEM-bilder bekrefter at batteriet fungerte normalt under CCC-målingene og gir innsikt i de termiske egenskapene og elektrokjemiske reaksjonene som oppstår i batteriet.

Utfallet av denne oppgaven bidrar til økt forståelse av de termiske egenskapene og kravene til termisk styring av litium-ionbatterier. Dette gir et godt grunnlag for videre forskning og undersøkelser av kjølesystemer som kan imøtekomme den økende etterspørselen etter litium-ionbatterier.

Preface

This thesis has been completed as a partial fulfillment of the requirements for the degree of Master of Science in Mechanical Engineering at the Norwegian University of Science and Technology (NTNU). It has been conducted as a project under the Department of Energy and Process Engineering (EPT) during the spring semester of 2023.

My deepest gratitude goes to my supervisor, Jacob Joseph Lamb, for believing in me and for giving his support and guidance throughout the project. I would also like to thank my co-supervisor, Markus Solberg Wahl, for his technical competence and invaluable help in the lab. I am truly grateful to them for sharing their knowledge, experience, and guidance. Also, the Research Council of Norway is acknowledged for the support to the Norwegian Micro- and Nano-Fabrication Facility, NorFab.

I would also like to express my heartfelt appreciation to Lena Spitthoff for dedicating her spare time and sharing her expertise with me. Her extensive knowledge of the theoretical background of Lithium-ion batteries (LiBs) and practical expertise in the lab has been incredibly valuable. The engaging conversations and her enthusiasm have greatly contributed to my motivation for the project.

On a personal level, I would extend my gratitude to my friends and fellow students for their support and motivation throughout this master's thesis. The fun times we shared have been truly cherished. A special thanks to my family for their endless love and support throughout my five years of study.

Silvia Athisayamohan
Trondheim, June 2023

Acronyms

Al	Aluminum
BoL	Beginning of Life
CCC	Cell Cooling Coefficient
CCCV	Constant Current Constant Voltage
Cu	Copper
DEC	Diethyl Carbonate
DMC	Dimethyl Carbonate
EC	Ethylene Carbonate
EDX	Energy Dispersive X-ray
EMC	Ethyl Methyl Carbonate
EPT	The Department of Energy and Process Engineering
EV	Electric Vehicle
HPPC	Hybrid Pulse Power Characterization
ICA	Incremental Capacity Analysis
LCO	Lithium Cobalt Oxide
LFP	Lithium Iron Phosphate or Lithium Ferro-Phosphate
LiB	Lithium-ion battery
LMNO	Lithium Manganese Nickel Oxide
NMC	Lithium Nickel Manganese Cobalt Oxide
NTNU	Norwegian University of Science and Technology
PC	Propylene Carbonate
PCM	Phase Change Material
PE	Polyethylene
PP	Polypropylene
pSEI	positive Solid Electrolyte Interphase
SEI	Solid Electrolyte Interphase
SEM	Scanning Electron Microscope
SoC	State of Charge
SoH	State of Health
TM	Transition metal
TMS	Thermal management system

Table of Contents

List of Figures

List of Tables

1 Introduction

This thesis builds on the foundation of the project work from the previous semester and the relevant contributions are cited.

1.1 Background

In recent years, Lithium-ion batteries (LiBs) have emerged as the leading energy storage technology, with the potential to play an important role in decarbonizing the global transportation and energy sectors. This popularity is due to their high gravimetric and volumetric energy, high power density, and high efficiency. As a result, they are commonly used in portable electronic devices and electric vehicles (EVs). LiBs can effectively convert chemical energy into electricity through chemical reactions, making them a clean and sustainable energy solution [1], [2].

Temperature is an important factor in extending battery life and increasing energy efficiency and overall performance. LiBs are known as high power performance batteries. However, they must operate at low temperatures and have effective heat dissipation to prevent overheating. In extreme cases, this can lead to explosions and fires. The heat generated during discharge and charge cycles increases the temperature of the battery, and over time, reduces the capacity and performance of the battery. In addition to considering the cooling requirements, it is important to focus on improving the production of LiBs to reduce greenhouse gas emissions and strengthen their sustainability. By improving the production phase of the LiBs, it is possible to minimize the emissions associated with LiB manufacturing while extending the lifespan and battery performance. The application of proper cooling systems is required to solve this problem [1], [3], [4].
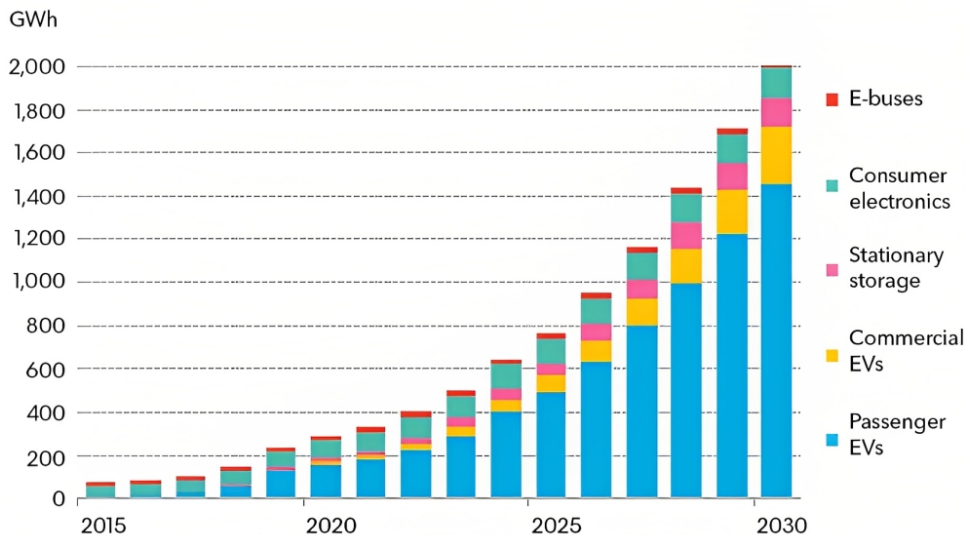
Figure 1: A graphical representation of the global demand for Lithium-ion batteries. Adapted from Bloomberg New Energy Finance (BNEF) [5].

Figure 1 represents a significant increase in the global demand for LiBs, especially in EVs for private and commercial purposes. The utilization of LiBs has in recent years, increased and is expected to reach 2.045 GWh by 2030, mainly due to the accelerated growth of EVs [5]. Meeting this growing interest will require improvements in thermal management systems (TMSs), which are critical for the safety and durability of battery packs. This demand results in rapid battery innovations which are mainly driven by energy and power targets. However, it is equally essential to improve the cooling capability of the battery in terms of thermal performance [3],[5], [6], [7].

1.2 The objective

The objective of this thesis is to investigate the cooling ability of beginning of life (BoL) LiBs. Previous research has been done by Hales et al. [6], who introduced the Cell Cooling Coefficient (CCC) which measures the ability of the cells to dissipate heat through surface and tab cooling. In addition, Christian Trandem and Colin MacDonald [8] conducted a master's thesis in 2021 investigating the impact of cooling methods on ageing LiBs. This study looks in-depth at how to effectively reject heat from the LiBs by focusing on different frequencies for the cooling setups. This is done by including thermal conductivity measurements, SEM images, and CCC measurements. This work is founded upon the methods and experiments conducted by Hales et. al, and MacDonald and Trandem, as their research contributes to the outline of this study.

2 Theory

A detailed theoretical knowledge of the thermal aspects and properties is required to understand the temperature measurements and cooling potentials. This chapter presents the basic working principles of a Lithium-ion battery (LiB) and the theory associated with the experiments conducted in this thesis.

2.1 Working principle of a Lithium-ion battery (LiB)

A lithium-ion battery (LiB) consists of two electrodes called anode and cathode, two current collectors, an electrolyte, and a separator, as shown in Figure 2. Each component is important because if one is missing or not functioning, the battery will not work [2]. A battery is a set of several interconnected individual cells [3].
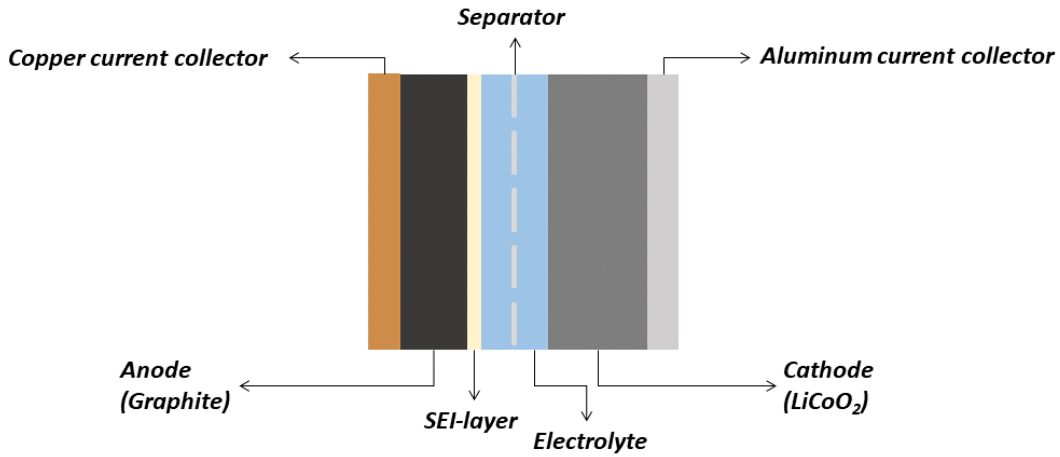
Figure 2: An illustration of a Lithium-ion battery (LiB). Inspired by Ismail et al. [9].

2.1.1 Electrodes

The electrodes of the battery are important components because of their critical roles in the performance and functionality of the battery. They are made of various materials that facilitate the electrochemical reactions that are required to generate electrical energy [2].

2.1.1.1 Anode

An anode in a LiB is the negative electrode that delivers lithium ions into the electrolyte. The anode material must be electrochemically active for oxidation reactions to occur in the battery. Examples of anode materials include carbon-based compon-

ents, silicon-based components, conversion materials and alloy materials or lithium metals [3], [10], [11].

The most commonly used anode material is graphite due to its low cost, high energy, power density and long cycle life. It can be called an intercalation material because the lithium ions intercalate to form LiC_6, and has been the dominant anode material in recent decades [12]. However, as seen in Figure 3, graphite has low capacity compared to silicon and has difficulty meeting the required energy density of today's batteries [3], [11].

Figure 3: A graphical overview of the average electrode potential against the specific capacity of the anode materials. Adapted from Nitta et al. [13].

As seen in Table 1, silicon has a high gravimetric and volumetric capacity. Silicon is not only quite affordable and abundant in the earth's crust, but it also makes an excellent anode material. However, some major obstacles limit the commercialization of silicon. For example, the possibility of capacity fade and degradation after cycling. Another major obstacle is the huge volume difference during the lithium-ion insertion or extraction processes. Through a conversion reaction, the silicon anodes are lithiated or de-lithiated. The huge volume differences lead to problems such as particle breakage, irregular and unstable electrical contact (delamination), repeated dynamic formation of SEI layers, and slow electron transfer. Low capacity, poor cyclability and lack of electrical conductivity are other reasons why silicon anodes are not commercially exploited and used in applications [3], [10], [11], [14].

Table 1: Anode chemistries

Anode	Theoretical Specific Capacity [mAh/g]	Experimentally achieved Specific Capacity [mAh/g]	Voltage (vs. Li/Li+) [V]	Sources
Graphite	372	350	0.05 - 0.2	[15], [16], [17], [18]
LTO ($Li_4Ti_5O_{12}$)	175	170	1.56	[15], [16]
Silicon Si-Alloys Si-(M)-C	4200 3580	3000 525 - 3163	0.05 - 0.6 -	[17], [19]
Lithium metal	3860	-	0	[15], [20]

Lithium metal has been discussed as an alternative anode material due to its high capacity and low electrochemical potential. However, lithium metal precipitates in dendric form during lithiation, which is the main cause of thermal runaway and explosion danger. Research has been conducted to improve the performance of lithium metal anodes. The use of electrolyte components, especially additives, change the anode surface and provide a uniform distribution of lithium ions [3], [21].

2.1.1.2 Cathode

A cathode is referred to the positive electrode that is reduced during discharge. Examples of cathode materials include Lithium Cobalt Oxide (LCO), Lithium Nickel Cobalt Manganese Oxide (NMC) and Lithium Iron Phosphate (LFP) [2],[3].

LCO is the most commonly used cathode material in LiBs. As seen in Table 2, it is a very attractive material due to its high specific and volumetric capacity, and good cycling performance. However, LCOs exhibit low thermal stability which favors the thermal runaway process (see Section 2.4.1.1.3), and faster capacity fade when operated at high current rates. In addition, this material is expensive due to the high cost of cobalt [3], [13].

Table 2: Cathode chemistries

Cathode	Theoretical Specific Capacity [mAh/g]	Experimentally achieved Specific Capacity [mAh/g]	Voltage (vs. Li/Li+) [V]	Sources
LCO ($LiCoO_2$)	274	106.5 - 160 180-190 (coated)	3.8 - 4.3 4.5-4.7 (coated)	[22], [23]
NMC111 ($LiNi_{0.33}Mn_{0.33}Co_{0.33}O_2$)	275	155-175	2.75 - 4.4	[24], [25]
LFP ($LiFePO_4$)	170	150 - 170	< 3.75	[26], [27]
LMO ($LiMn_2O_4$)	148	120 - 130	3.8 - 4.2	[25], [28]
LNMO ($LiNi_{0.5}Mn_{1.5}O_4$)	147	117 - 137	4.7	[29], [30] [31]

In addition, NMC has an equal or higher specific capacity than LCO and operates at the same voltage. This material is less expensive compared to LCO because the Cobalt is reduced. The most commonly used form of NMC is $LiNi_{0.33}Mn_{0.33}Co_{0.33}O_2$, and some NMC chemistries are being studied due to faster capacity fade and shorter lifetime compared to the most commonly used [3], [11], [13], [24].

Another representative material used as a cathode is LFP, due to its thermal stability, low operating voltage, and volumetric energy density, as shown in Figure 4. Unfortunately, some limiting factors include its relatively low average potential and low electrical and ionic conductivity. LFP is still attractive due to its high performance and high safety level [3], [11], [13].
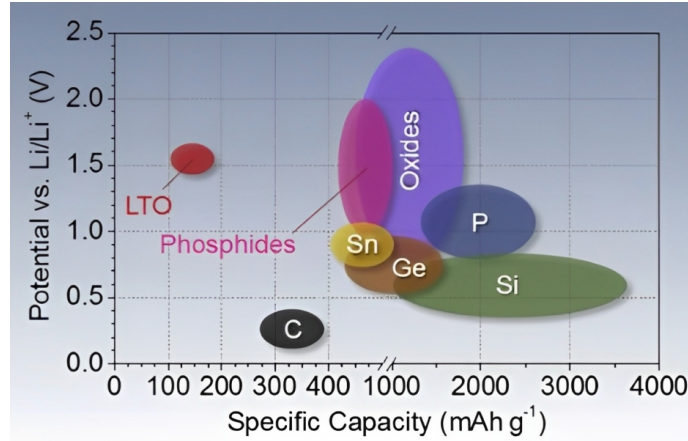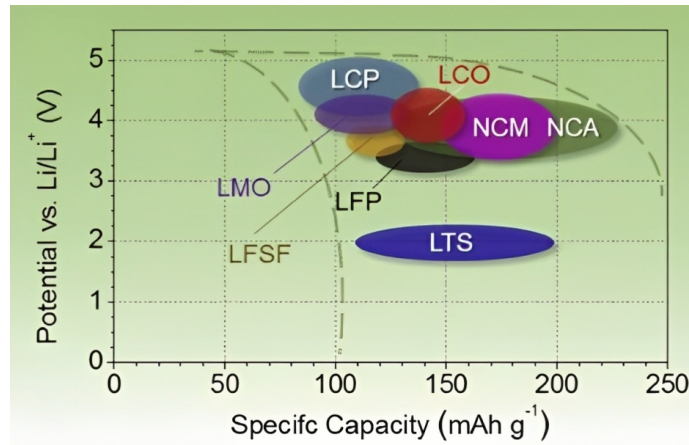
Figure 4: A graphical overview of the average electrode potential against the specific capacity of cathode materials. Adapted from Nitta et al. [13].

2.1.2 Current collectors

A current collector is a metal film that lowers the resistance when electrons are moving to the carbon (anode). Most lithium-ion batteries have one current collector for each electrode. Current collectors operate as a bridge, where they connect the collected electrical current, which is generated at the electrodes, to the external circuits. Aluminum (Al) and copper (Cu) foils are often used as commercial current collectors for cathodes and anodes (Al for the cathode and Cu for the anode). Current collectors must be electrochemically stable, therefore copper and aluminum are mostly used because of their stability and electrical conductivity. The effectiveness of LiBs can be significantly impacted by current collectors, for instance, increasing the electrical conductivity and reducing the contact resistance [2], [3], [32].

Zhang et al. [33] employed an electrochemical-electrical-thermal coupled modeling approach to study the heat generation in current collectors by analyzing the distribution of current density in the battery cell. The tab connections to the current collectors create an external terminal connection. Therefore, with high electrical and thermal conductivity, tab cooling can be effectively used to dissipate thermal energy from the battery [8].

2.1.3 Electrolyte

The electrolyte is the component that interacts with the other components in a battery and therefore determines the stability of cycling, power density and safety of the battery. In most electrolytes, lithium salt is present which helps lithium ions to move conductively due to the presence of $LiPF_6$, $LiBF_4$, $LiClO_4$ in various organic solvents. Examples of organic solvents include Propylene Carbonate (PC), Ethylene Carbonate (EC), Ethyl Methyl Carbonate (EMC), Dimethyl Carbonate (DMC), and Diethyl Carbonate (DEC). When the cells are exposed to air, the extremely flammable electrolyte solutions pose a serious risk of fire and explosion danger. Unlike wet batteries, the liquid electrolyte does not flood the battery cell.

The active components of the cell absorb it. Polymer is another type of electrolyte. Polymer electrolyte has a significant weight advantage over liquid electrolyte. It is also less flammable and more flexible. However, polymer is more susceptible to mechanical stress and has lower ionic conductivity [2], [3], [32], [34].

2.1.4   Separator

A separator is a porous material with a thickness of 20 micrometers. Commonly used materials are microporous polyolefin membranes such as Polyethylene (PE), Polypropylene (PP), or composite membranes because of their mechanical properties, electrochemical stability and affordability. These materials are used to separate the anode from the cathode. Figure 5 shows a schematic representation of a separator between the two electrode materials and the separator is much smaller than the electrodes. This is to avoid direct contact, short circuits, and overheating known as thermal runaway. This is explained in more detail in Section 2.4.1.1.3. The separator ensures that the electrodes are electrically separated, but allows the lithium ions to pass through. However, the commercially available separators have low thermal stability, which can be a safety risk when overheated. The high temperature causes the separator to shrink and become incapable of preventing an internal electrical short circuit rendering the battery inoperable. Therefore, the thermal issues must be considered due to the separators´ thermal stability being directly related to the safety of LiBs. Figure 5 shows the construction and different component thicknesses in a LiB [2], [3], [35].
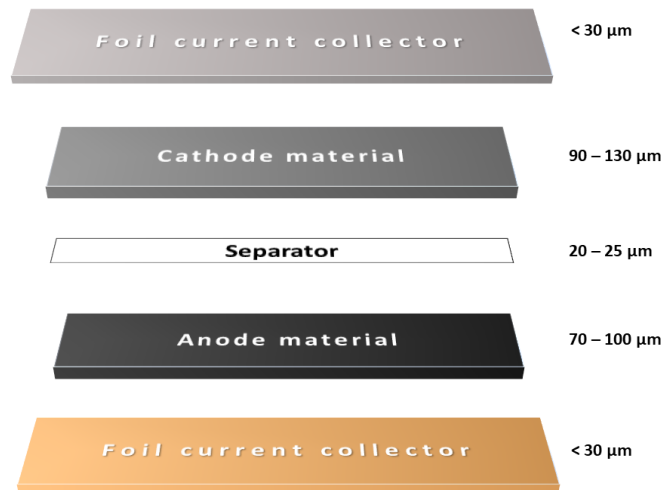
Figure 5: A schematic of each component and their sizes in a Lithium-ion battery (LiB). Inspired by Wahl et al. [36].

2.1.5   Solid Electrolyte Interphase (SEI)

The SEI or the solid electrolyte interface is a passivation layer that forms around the anode particles during the first cycle of the battery. This high resistance layer forms

between the anode and the electrolyte to prevent the lithiated anode from coming into contact with the electrolyte. The interfacial layer is a critical factor, because it allows the lithium ions to penetrate inside the graphite anode, turn into lithium metal, and deposit on the surface of the anode. Not only is this layer required, but it also keeps expanding and eventually reduces the battery performance [2], [3], [37], [38].

2.1.6 Reactions

LiBs rely on a crucial process called intercalation, where energy is generated by the movement of lithium ions between the anode and cathode materials. The drift of electrons sets the potential for the amount of energy a LiB can generate. This is caused by redox reactions in the cathode and anode materials. When the LiB is charged, lithium ions deintercalate from the cathode, diffuse through the separator, and eventually intercalate into the anode. During discharge, the reaction reverses, i.e., the lithium ions deintercalate from the anode, resulting in free electrons. These free electrons drift through an external circuit to produce energy. The free lithium ions return to the cathode material through the separator. Figure 6 shows the working principle for a LiB during discharge and charge [3], [11], [14], [32], [39].
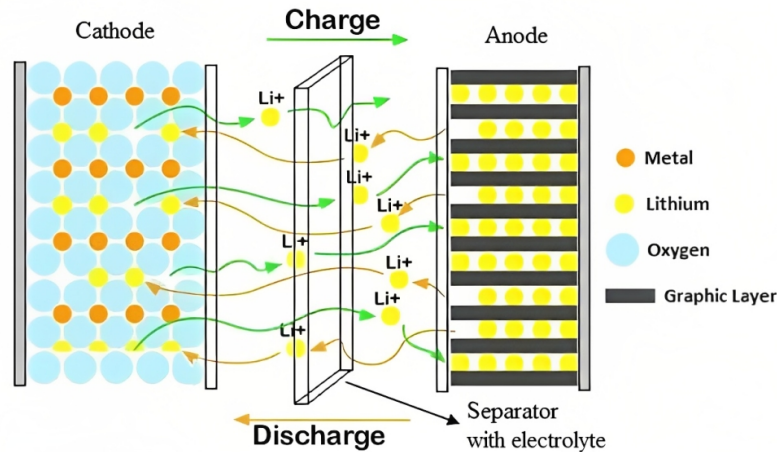
Figure 6: An illustration a Lithium-ion battery (LiB) during discharge and charge. Adapted from Hannan et al. [40].

An LCO battery is used as a baseline when referring to LiBs. The redox reactions that take place during the charge and discharge in this battery can be defined by these chemical reactions [3], [41]:

Negative electrode: $xLi^+ + xe^- + 6C \rightleftarrows Li_xC_6$
Positive electrode: $LiCoO_2 \rightleftarrows Li_{1-x}CoO_2 + xLi^+ + xe^-$
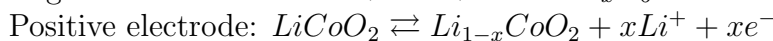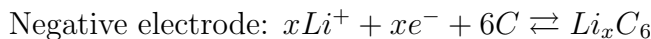
The total reaction of the battery is expressed as [41]:

Total: $LiCoO_2 + 6C \rightleftarrows Li_{1-x}CoO_2 + Li_xC_6$

2.2 General terminology

2.2.1 C-rate

The C-rate is the unit used to measure the speed when a battery is fully charged or discharged [42]. In particular, it provides information about the current the battery can deliver or receive. For example, charging at a C-rate of 1C means the battery is charged from 0% state of charge (SoC) to 100% SoC in one hour, corresponding to one full cycle [2]. Equation 1 shows this relationship between the current and the nominally rated energy, which equals the C-rate [3], [8], [43].

$$C = \frac{I \ [A]}{Q_{\text{rated energy}} \ [Ah]} \tag{1}$$

2.2.2 State of Health (SoH)

The term state of health (SoH) describes the condition of the battery compared to its ideal condition, as shown in Equation 2 [8]. As batteries lose capacity during ageing, the SoH value decreases. The SoH value is determined by the charge available at a given C-rate compared to the charge of a new battery, which must be measured at the same C-rate and temperature, as these are important factors defining the battery capacity [2], [3].

$$SoH = \frac{\text{Capacity at current state when fully charged [Ah]}}{\text{Capacity under ideal conditions [Ah]}} \times 100 \tag{2}$$

2.2.3 State of Charge (SoC)

State of charge (SoC) is a percentage measure of the energy available in a battery at a given time relative to its design capacity [2]. This relationship is presented in Equation 3 [3], [8].

$$SoC = \frac{\text{Available charge left [Ah]}}{\text{Capacity at 100\% SoC [Ah]}} \times 100 \tag{3}$$

2.2.4 Constant current constant voltage (CCCV)

The most commonly used charging strategy for a LiB is constant current constant voltage (CCCV), where the charging protocol is charged at a constant current until

a certain voltage is reached. This process is necessary to avoid overcharging. Then, when a constant voltage is reached, the charge current is decreased [44]. This process is shown in Figure 7.
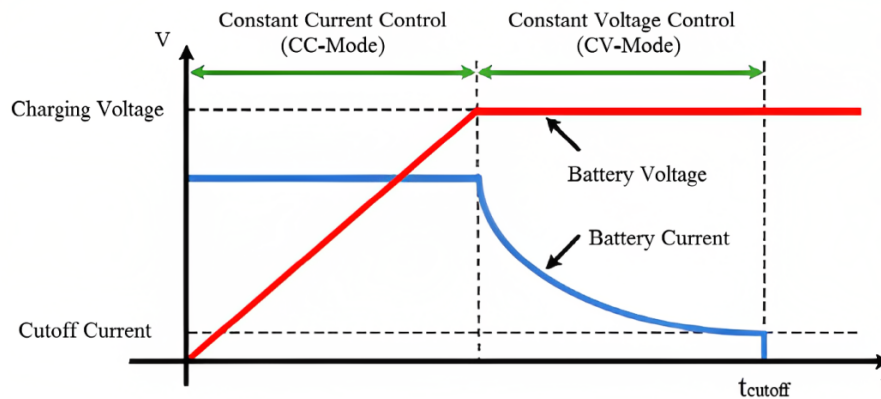
Figure 7: Constant current constant voltage (CCCV) battery charge. Adapted from Jadav [45].

2.3 Thermal aspects and properties of Lithium-ion batteries (LiBs)

2.3.1 Heat generation in Lithium-ion batteries (LiBs)

Heat generation in LiBs at ambient temperatures is primarily due to charge transfer and chemical processes during charge and discharge cycles. LiBs can generate heat by either an irreversible or a reversible process. Figure 8 shows the primary heat generation processes in a LiB [3], [46].
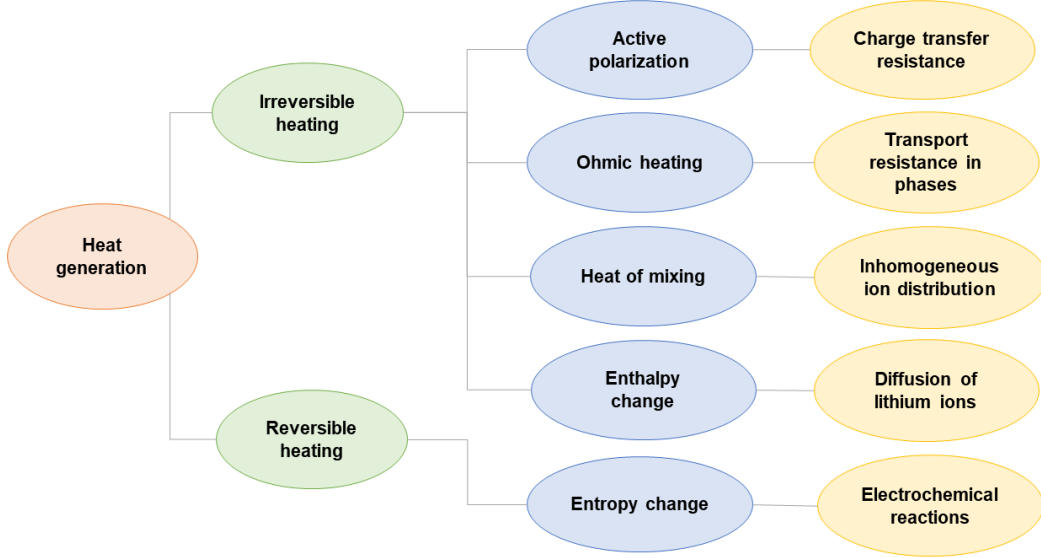
Figure 8: An illustration of heat generation processes in a Lithium-ion battery (LiB). Inspired by Ma et al. [46].

Even though the efficiency of converting chemical energy into electrical energy is high, there is still energy loss in the form of heat. In the electrochemical cell, there are three primary sources of heat generation: Ohmic heat, q_{ohmic}, Tafel heat, $q_{overpotential}$, and heat due to entropic changes, $q_{entropy}$, which occur during electrochemical reactions. This relation is described in Equation 4. All of these sources depend on current density [47]. In this section, the two heat generation processes are briefly described [3], [48].

$$q_{cell} = q_{entropy} + q_{ohmic} + q_{overpotential} \qquad (4)$$

1. Entropic heat is the reversible source of heat. It arises from a rearrangement in the electrode and acts as a heat source when discharging and as a heat sink when charging [3], [36], [49].

2. Ohmic heat is generated by ion transport in the electrolyte and electron transport between electrode surfaces. It is given by the specific ohmic resistance, r_w, and the current density j, which is equal to $r_w j^2$ [3], [36], [47], [48], [50].

3. The overpotential is due to reduced cell potential, which is caused by the resistance to the electrochemical reactions. This is given by the overpotential, η, and the current density, j, which is equal to ηj [3], [36], [48], [51].

These equations represent the total heat generation of a LiB during charging and discharging [3], [48], [52], [53].

$$q_{charge} = \frac{T \cdot \Delta S}{F} j + r_w j^2 + \eta j \qquad (5)$$

$$q_{discharge} = -\frac{T \cdot \Delta S}{F} j + r_w j^2 + \eta j \tag{6}$$

2.3.1.1 Irreversible heating

Some irreversible processes contributing to heat generation are active polarization, ohmic heating, and heating due to the change in mixture enthalpy. The polarization process results from the overpotential between the operating potential of the batteries and the open circuit potential. As a result, the charge transfer resistance at the electrode-electrolyte interface or SEI increases. Heat is generated as the lithium ions overcome this resistance at the interface for their intercalation or deintercalation. An ohmic heating process takes place in both the electrode and the electrolyte. Electrodes and electrolytes have a high resistance that prevents charges from moving. The ion distribution in LiBs becomes inhomogeneous during operation, either charging or discharging. This causes the ions to mix, resulting in heat generation. When lithium ions diffuse, an enthalpy change occurs due to the cathodes' phase change. This irreversible process also leads to heat generation. The irreversible process can be described by Equation 7 or 8 [3], [11], [46].

$$Q_\eta = \eta_{battery} \cdot I \tag{7}$$

$$Q_\eta = I^2 \cdot R \tag{8}$$

In Equation 8, R represents the internal battery resistance, which is a crucial factor for heat generation [3], [11].

2.3.1.2 Reversible heating

The reversible entropy change that occurs in electrochemical processes is the source of the heat generated in the reversible process, also known as entropic heat. This can be calculated using Equation 9. This heat from the reactions is affected by SoC and is either exothermic or endothermic depending on whether the battery is being charged or discharged [3], [11], [36], [52].

$$Q_s = -\frac{T \cdot \Delta S}{n \cdot F} \cdot I \tag{9}$$

Here, Q_s refers to the reversible reaction heat, F is the Faraday constant, and ΔS is the change in entropy [3], [11] [54].

2.3.2 Heat rejection in Lithium-ion batteries (LiBs)

To improve battery performance, LiBs must be cooled down. Various approaches such as air cooling, liquid cooling, and Phase change material (PCM) cooling technologies are discussed in this subsection in addition to the cooling method used in this thesis [3], [55].

2.3.2.1 Air cooling

Air cooling is the usual method of removing heat from batteries. This is done either by natural convection using air cooling or by forced convection using a fan, which is most commonly used to cool the battery. Simplicity and affordability are some of the advantages of these methods. However, the disadvantage of natural convection is uncontrollable wind, which weakens the ability to remove heat from the batteries [55].

2.3.2.2 Liquid cooling

Another widely used cooling method is liquid cooling. This method is more effective than air cooling in removing heat, because the heat transfer coefficient of water is higher. Liquid cooling can be done in two ways: direct cooling and indirect cooling. Direct cooling improves the temperature uniformity of a LiB by cooling the battery surface. However, this method requires a waterproof system to prevent leakage of the cooling liquid. In addition, it requires carefulness due to electrochemical reactions and electrical short circuits that can occur. In contrast, indirect cooling, such as tube cooling and cold plate cooling, is safer and easier to implement. Unfortunately, this method is more complex than air cooling [55].

2.3.2.3 Phase Change Material (PCM) cooling

PCM cooling is a method that does not require additional energy. Materials that can absorb and release large amounts of heat are used in the thermal management systems (TMSs) of the battery to keep the temperature in a safe range through passive cooling. The PCM work by having the material change phase, from solid to liquid, thereby reducing the temperature of the battery. Heat is absorbed during the phase change, which is an effective way of cooling the battery [8], [55].

2.3.2.4 Cell Cooling Coefficient (CCC)

As mentioned in Section 1.2, in this study, the work of Hales et. al. [6] and Trandem and MacDonald [8] have been used as a foundation. Hales et al. [6] introduced a new metric that can be used to quantify the heat rejection rate. It is called the

Cell Cooling Coefficient (CCC) and helps to evaluate the thermal performance of different cooling systems. The CCC also allows comparison of the thermal paths within each cell design by looking at components such as underlying chemistry and geometry, form factor, and internal thermal gradient. A cell has a higher capacity when the thermal gradient within the cell is low. This cell has a high CCC value because a large amount of continuous energy can be used from the cell. When a cell has a high CCC value, it means that the average cell temperature is relatively low and this cell has a long lifetime in combination with a low thermal gradient. The concept of thermal gradients will be elaborated further in the next subsections [3], [6], [7].

$$CCC = \frac{\dot{Q}}{\Delta T} \tag{10}$$

In Equation 10, the CCC is defined, where $\dot{Q}$ represents the heat rejected from the selected surface or tab, and ΔT is the temperature difference between the hottest part inside the cell and the surface when it is cooled down. It is measured in units of $\frac{W}{K}$. This method is explained in detail in Section 3.2 [3], [8], [6], [7].

2.3.3 Thermal conductivity

Thermal conductivity differs from one material to another. For example, heat transfer by conduction is higher in metals than in wood. This value depends on the atomic and molecular structure of the matter [48], [56]. Bergman et al. [56] explain that the thermal conductivity of a material, also defined as a transport property, refers to the ability of the material to conduct heat. A low thermal conductivity means the material does not conduct heat well [3], [48].

Fourier's law describes the conductive heat flux as [11], [56]:

$$\mathbf{q} = -k \ \cdot \nabla T \tag{11}$$

Here, ∇T is the temperature gradient and k is the thermal conductivity expressed as W/mK.

In batteries, thermal conductivity is described as non-isotropic and inhomogeneous due to the battery cell design and depends on the direction of the cell. The terms "in-plane" and "cross-plane" are commonly used [8], [53], [56]. An effective heat transfer coefficient can be used to determine the conductivity of the different layers of the battery [3], [11].

The heat transfer coefficient in the cross-plane direction can be defined as [8]:

$$k_{eff\ cross-plane} = \frac{d_{cell}}{\sum \frac{d_i}{k_i}} \tag{12}$$

And the heat transfer coefficient in the in-plane direction can be defined as [8]:

$$k_{eff\ in-plane} = \frac{\sum k_i \cdot d_i}{d_{cell}} \tag{13}$$

Here, k_i is the thermal conductivity of the individual battery components, d_i is the component thickness, and d_{cell} is the total thickness of the battery [3], [8], [11], [53].

In addition, Spitthoff et al. explain that thermal conductivity is important, as it defines the heat transport in the battery, which is important for dimensioning efficient cooling systems such as the CCC rigs used in this thesis.

2.3.4 Thermal gradients

Temperature gradients are formed inside the LiB during operation due to internal heat generation and the low thermal conductivity of the battery. These gradients are often noticeable at higher C-rates, where heat is generated faster than it can be dissipated out to the surroundings. An example of these gradients in a pouch cell can be seen in Figure 9. Due to the higher internal resistance, creating cells with high volumetric energy density and a large amount of active material results in larger thermal gradients. The TMS must provide sufficient cooling to compensate for the internal heat generation [3], [11], [57].
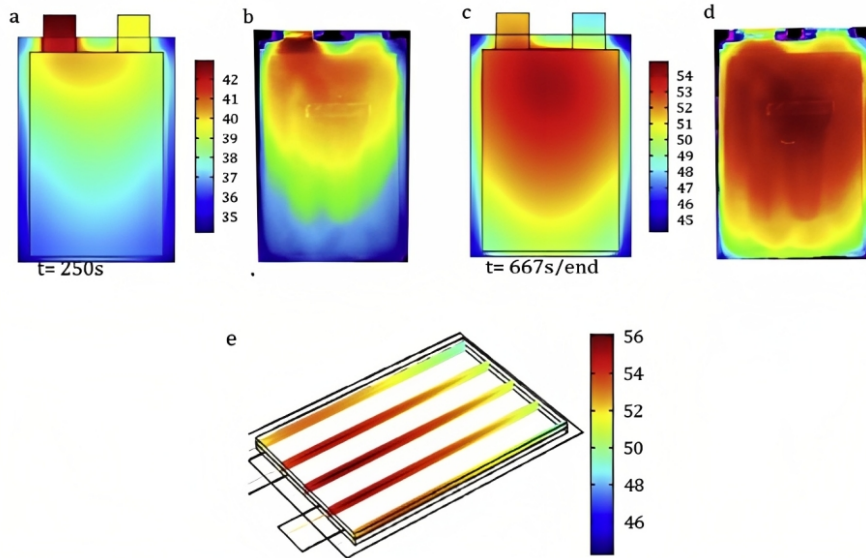
Figure 9: An illustration of how the surface temperature in a pouch cell changes during discharge. Adapted from Tomaszewska et al. [58].

2.3.5 Scanning Electron Microscope (SEM)

Scanning electron microscope (SEM) is a commonly used instrument for imaging the surface structure and morphology of various materials. The use of a focused

beam to generate images allows clear visualization of surface features through high-resolution images. These are valuable for evaluating properties such as particle size, shape, distribution, and structural integrity of battery electrodes. To study the transport of thermal energy by ions and electrons in the material, particle size is an important factor. In addition, particle size can affect the uniformity of thermal energy transport and packing density, which affects the overall battery performance. The surface features of the electrodes are also of interest, as signs of cracks, pores, and dendrites can reveal ageing or degradation [59].

2.4   Ageing and degradation

2.4.1   Parameters affecting the degradation

2.4.1.1   Changes in temperature

It is scientifically proven that temperature has a significant impact on the performance and ageing mechanisms of a LiB. In addition, temperature control is critical to avoid safety issues, such as thermal runaway and dendrite growth. As shown in Figure 10, LiBs function optimally in the range between 15℃-35℃, but this may vary for different battery chemistries [3], [11], [46]. Most temperature effects are caused by chemical processes inside the batteries and the materials used in the batteries. In addition to chemical processes, temperature affects the ionic conductivities of electrodes and electrolytes [3], [11], [46].
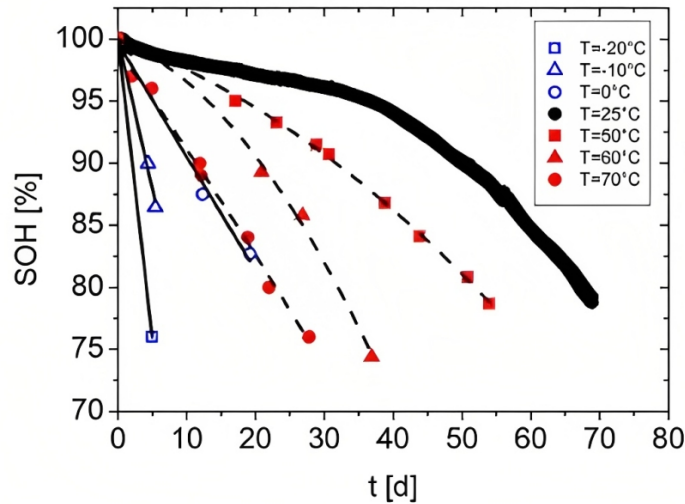
Figure 10: State of Health (SoH) curves as a function of time for cycling at different temperatures and 1C. Adapted from Waldmann et al. [38].

2.4.1.1.1   Effects of low temperature

When operating at temperatures below 0℃ the quality of LiBs performance decreases. The performance decrease at low temperatures can have a variety of causes due to the complicated material system used in LiBs. First, the properties of the electrolyte are affected by the low temperature. The ionic conductivity decreases as the temperature drops because the viscosity of the electrolyte increases. Another cause of performance degradation due to low temperature is the increase in charge transfer resistance in LiBs at the graphite anode or SEI layer [3], [46].

Lithium plating is another consequence of low temperatures. The cold circumstances cause the anodes to become polarized, and the potential of graphite and other carbon-based anodes to approach that of lithium metal and slow the intercalation of LiBs into the anodes during charging. This results in the accumulated lithium ions being deposited on the electrode surfaces, reducing battery capacity. In addition, the lithium plating gets a dendritic form, which can puncture separators and cause an internal short-circuit [3], [46].

2.4.1.1.2 Effects of high temperature

According to Ma. et al. [46] the consequences at high temperatures are far more complex compared to low temperatures. When LiBs are in operation, heat is generated inside the batteries. Therefore, understanding heat generation is crucial to prevent the effects caused by high temperatures in LiBs [3], [46].

2.4.1.1.3 Thermal runaway

Heat is generated when LiBs are discharged. When the temperature of the battery cells exceeds a certain threshold, the cells enter a condition known as thermal runaway. Thermal runaway means that the temperature in the cell continues to rise until it either ignites or is mechanically destroyed. Therefore, keeping the cell temperature within the specified temperature range from the manufacturer is essential. Most batteries have a venting mechanism that is designed to dissipate heat from the cells and prevent the batteries from catching fire or exploding. Unfortunately, the battery cannot be used after the venting mechanism has dissipated the heat and the battery has cooled [2], [3], [34], [43].

2.4.1.2 Changes in C-rate

The LiB may degrade when the C-rate increases, as higher C-rates result in a higher thermal gradient. A high C-rate also makes it easier to distinguish between tab and surface cooling, when it comes to avoiding degradation [3], [6], [8], [60].

2.4.1.3 Changes in State of Charge (SoC)

MacDonald and Trandem [8] describe that there are two types of degradation processes caused by SoC. First, when the SOC is increased, the materials move outside the stable voltage window, which catalyzes specific reactions, particularly with the electrolyte. Second, when the cell operates at these states of charge, the electrodes become either fully or partially lithiated, resulting in structural stresses [3], [8].

2.4.2 Ageing mechanisms

Ageing is a consequence of the application of LiBs at high temperatures. Ageing of LiBs affects both performance and lifetime, and the ageing process accelerates when the operating temperature of LiBs increases beyond the ideal range [46]. Furthermore, the ageing mechanisms strongly depend on the compositions of the electrodes and vary for the anode and cathode [1]. Vetter et al. [61] explain that the ageing processes of LiBs are complicated systems to understand. Since capacity fading and performance degradation are caused by several processes and their interactions, these processes need to be studied together. As the ageing is different for anode and cathode and their active materials, they are discussed in two separate subchapters [3], [61].

2.4.2.1 Ageing of carbon-based anodes

The main anode material used in LiBs is carbon, especially graphite. Therefore, researchers have gotten a better understanding of anode ageing by using graphite cells. The ageing effects on the graphite anode can lead to characteristic changes in the cathode over time and usage. The calendar life of the battery is affected by ageing effects that occur during storage, such as impedance rise and self-discharge. Cycle life is also affected by ageing effects that occur during use, such as mechanical degradation and lithium metal plating. Ageing over time can result in or be caused by changes in the electrode and electrolyte, active materials, and composite electrodes such as current collectors, active materials, conductive additives, binders, porosity, etc. Ageing effects may be primarily related to electrode or electrolyte interface changes. This will be discussed further in the text [3], [61].

2.4.2.2 Ageing of lithium metal oxide cathodes

Cathode materials significantly impact cell performance, cycling and calendar life of LiBs. Some changes that occur at the cathode are:

- Ageing of the active material

- Interaction between the negative electrode and ageing products

- Surface film formation and oxidation of electrolyte components

- Changes in electrode components such as binders, conducting materials and corrosion of current collectors

These consequences depend on the electrode composition and occur due to cycling and storage conditions. In addition, the charge capacity fading in the cathode results from either structural changes under cycling, changes on the surface film or chemical decomposition reactions. Figure 11 provides an overview of the causes and consequences of cathode ageing, as mentioned in this paragraph [3], [61].
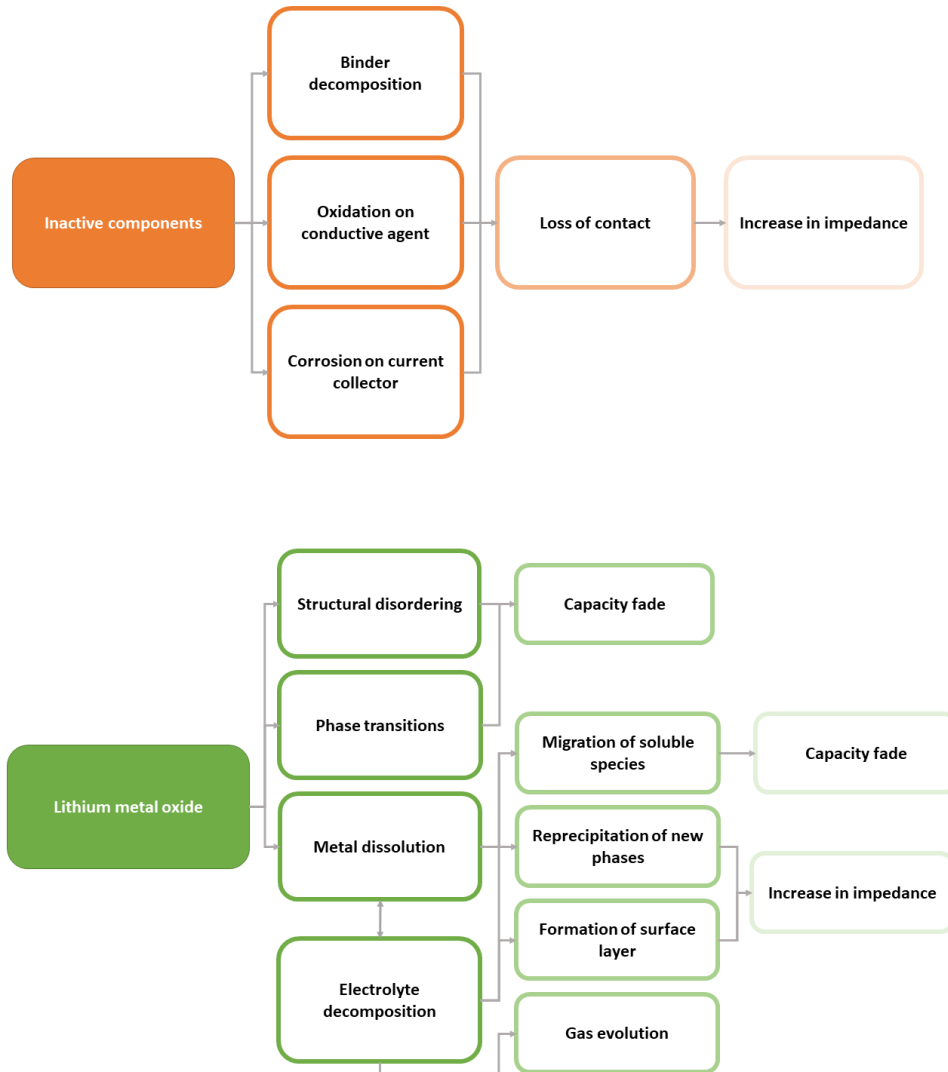
Figure 11: An overview of ageing mechanisms which occur on the cathode. Inspired by Vetter et al. [61].

2.4.3 Degradation mechanisms

A good understanding of how battery degradation works is important for the cost-effective decarbonization of transportation and energy systems. Many physical and

chemical mechanisms lead to the degradation of LiBs. These mechanisms involve the various components of a battery, including electrodes, electrolytes, separators, and current collectors. See Figure 12 for an illustration showing various degradation mechanisms. This subsection covers the common degradation mechanisms in a LiB [3], [62], [63].
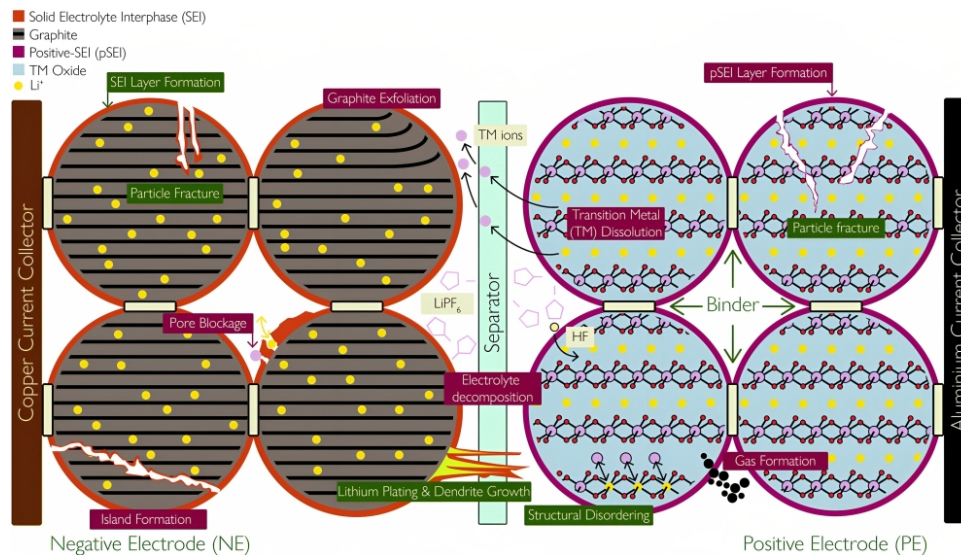
Figure 12: An overview of the degradation mechanisms which occur in a Lithium-ion battery (LiB). Adapted from Edge et al. [62].

2.4.3.1 Loss of lithium inventory

Birkl et al. [63] explain lithium-ion loss due to other reactions such as SEI layer growth and lithium plating. When lithium ions are no longer available for cycling, it can lead to reduced performance and a reduction in the maximum capacity that can be extracted from the battery. In addition, loss of lithium inventory can also occur if the lithium ions are trapped in electrically isolated particles of active material [3], [64].

2.4.3.2 Solid Electrolyte Interphase (SEI) layer growth

As mentioned in Section 2.1.5, SEI is a passivation layer found on most negative electrode surfaces. It forms when a liquid electrolyte comes into contact with the electron-conducting surface of the negative electrode. This often occurs at voltages outside the electrochemical stability window of the electrolyte. As a result, redox reactions are irreversibly accelerated, the electrolyte decays and electrolyte losses occur. Both lithium metal electrodes and graphite form this SEI layer. As shown in Figure 13, this layer has been shown to contain several chemicals, including Lithium fluoride (LiF), Lithium carbonate ($Li2CO3$), Lithium methyl carbonate ($LiOCO_2CH_3$) and Lithium oxide (Li_2O) [3], [62].
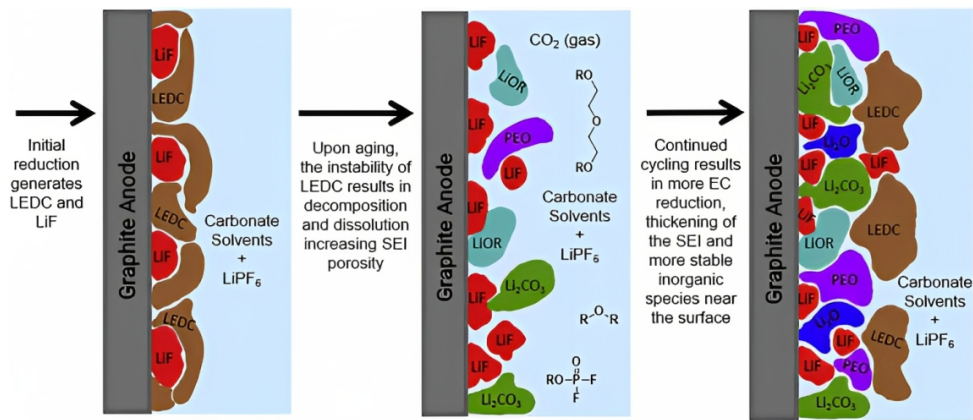
Figure 13: A schematic of Solid Electrolyte Interphase (SEI) formation. Adapted from Heiskanen et al. [65].

The SEI forms within the first cycle and increases at high temperatures and currents. In addition, the thickness of this layer increases as the battery ages, as seen in the figure above, which can have many causes. These include diffusion of solvent molecules across the layer, contact with new electrode surfaces due to cracking, and products from other side reactions [3], [62].

2.4.3.3   Lithium plating

Edge et al. [62] explain that lithium plating can be caused by low temperatures, high SoC, high (charge) current, high cell voltage, or by an electrochemically active surface area. In the side reaction, known as "Li plating," the formation of lithium metal occurs on the surface of the negative electrode instead of intercalating into it. Figure 14 shows the formation of lithium plating on the anode. This occurs as a result of rapid charging, where the high electrolyte potential accelerates the side reaction relative to the main intercalation reaction, also known as kinetic plating. "Li plating" can also occur when the surface of the negative electrode is fully lithiated, so that the lithium ions have nowhere else to go, also known as thermodynamic plating. Low temperatures slow the primary intercalation reaction sufficiently, making plating happen even at a moderate charge rate. The reverse reaction, stripping, can recover the lithium metal, as with any other electroplating procedure [3], [62].
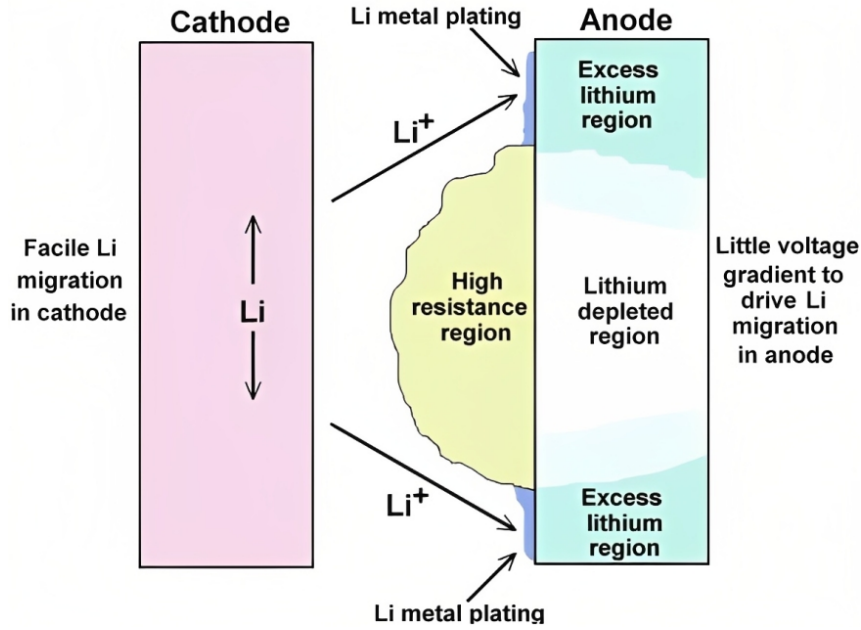
Figure 14: An illustration of the Lithium plating reaction. Adapted from The Aerospace Corporation [66].

2.4.3.4 Structural changes and decomposition in electrodes

The other three degradation mechanisms mentioned in this section affect the negative electrode more than the cathode. Nevertheless, the cathode is affected during degradation. The chemistry underlying the degradation of the positive electrode is quite complex. Various transition metal (TM) oxide materials are used as positive electrodes in LiBs, including layered oxides such as LCO and NMC, spinels, and polyanion oxides. The focus is on layered oxides, especially NMC-based positive electrodes, as they provide one of the highest achievable energy densities and are among the top positive electrodes in today's applications. NMC-based positive electrodes differ from the others due to the different ratios of nickel, cobalt, and manganese that are used in the different cells. Each of the abovementioned cathode materials plays a vital role in the ageing and degradation of the positive electrode [3], [62].

2.4.3.5 Particle fracture

A particle fracture can be seen in both electrodes. It is caused by the significant volume change of the electrode materials and the stress resulting from the electrochemical action. According to Edge et al. [67], local fragmentation of particles near the separator was observed as the greater local current densities produce a higher amount of stress. Particle fracture is complicated in active materials with a high theoretical specific capacity, such as silicon [3].

Edge et al. [62] explain several effects of cracks in electrode particles:

- Interrupts the electrical contact between the active particles, conductive additives, and the current collector, ultimately leading to loss of electronic or ionic conductivity and capacity fade.

- Particles more extensive than a specific critical size can break into many isolated islands.

- Electrode pulverization occurs when tiny cracks in the electrode cause the active material to detach from the particles. This leads to a loss of active material and, subsequently a drop in capacity.

- Increased growth of SEI and positive Solid Electrolyte Interphase (pSEI). The abovementioned three consequences all lead to a decrease in capacity.

2.5 Melasta SLPBB042126

In this thesis, there has been used a LCO battery which has a high energy density. Shenzhen Melasta Battery Co Ltd manufactures this cell, and the technical specifications of this cell are presented in Table 3. In addition, a comprehensive datasheet can be found in Appendix A[68]. It is also worth mentioning that this cell serves as the primary battery for the Norwegian University of Science and Technology (NTNU) electric race car, known as Revolve [3].

Table 3: Cell specifications for Melasta SLPBB042126 [68].

Parameters	Value	Unit
Nominal Voltage	3.7	[V]
Nominal Capacity	6550	[mAh]
Internal resistance	≤ 1.5	[mΩ]
Charge Voltage	4.2	[V]
Charge Cut-Off Voltage	4.2	[V]
Discharge Cut-Off Voltage	3.0	[V]
Operating charge temperature	0 to 45	[$^\circ C$]
Operating discharge temperature	-20 to 60	[$^\circ C$]
Weight	126.0 $\pm$3.0	[g]

2.6 Aims of this work

The aim of this thesis is to study the effects of changes in frequency and C-rate during cycling in different cooling systems and how these parameters affect the thermal properties of the LiBs. With a deeper understanding of these changes, an intelligent TMS can be dimensioned. Therefore, cooling methods such as surface cooling and tab cooling are investigated to study the heat rejection and lifetime extension of LiBs [3], [7].

3   Methodology

This chapter presents schedules and methods used to characterize the batteries and to obtain the Cell Cooling Coefficient (CCC). In addition, this study covers thermal conductivity measurements and Scanning Electron Microscopy (SEM) to understand the influence of chemical and thermal properties on the CCC.

3.1   Cell characterization

Prior to the Cell Cooling Coefficient (CCC) measurements, characterization tests were performed on the cells with an Arbin LBT battery tester. The characterization began with discharge and charge cycles at various C-rates, followed by hybrid pulse power characterization (HPPC). These tests were performed to evaluate the changes in battery capacity and the internal resistance of the battery [3], [8], [11].

The following schedule shows the characterization performed on each battery:

- Discharge and charge at 1C

- Discharge and charge at C/20

- Discharge and charge at C/4

- Hybrid pulse power characterization (HPPC) at different states of charge (SoCs)

- Discharge at 1C, C/4, C/10 and C/20

An HPPC was employed to investigate the internal resistance at various states of charge (SoCs). The voltage response of the battery, ΔV, determines HPPC due to a step-current discharge pulse, ΔI. An example is shown in Figure 15 [3], [69].
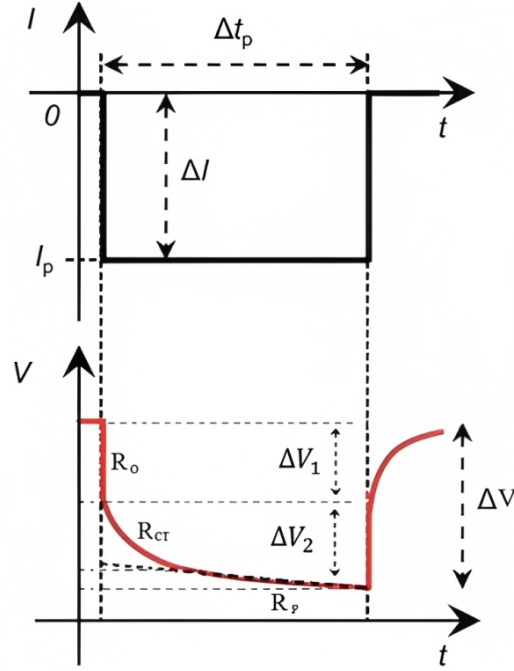
Figure 15: An illustration of a hybrid pulse power characterization (HPPC) test. The upper figure shows the step-current pulse, ΔI, while the lower figure shows the voltage response, ΔV. Adapted from Barai et al. [69].

The time step used in the HPPC test is a dependent factor when measuring the voltage change. When applied current, the ohmic overpotentials cause the initial voltage drop in the battery. This is referred to as R_o in Figure 15. The charge transfer resistance, which is a result of the charge transfer reaction at the electrode, causes the voltage drop within the next few seconds, R_{CT}. Subsequently, the voltage drops further due to changes in the lithium surface concentration of the active mass particles. Finally, the voltage drops even further because of the polarisation resistance, R_p, where ionic diffusion occurs in the solid phase, and also determines the rate of lithium-ion batteries [3], [11], [69], [70].

In this thesis, the HPPC tests conducted for the voltage measurements were performed at two time intervals: 50ms and 5s. The first measurement at 50ms reflects the influence of the ohmic resistance R_o. Following, the resistance measured between 50ms and 5000ms covers the voltage drop of both charge transfer resistance and polarization resistance. These factors are calculated as follows [8], [11]:

$$R_{IR} = \frac{\Delta V_0}{\Delta I_0} = \frac{V_{0ms} - V_{50ms}}{I_{0ms} - I_{50ms}} \tag{14}$$

$$R_{CT} = \frac{\Delta V_1}{\Delta I_1} = \frac{V_{50ms} - V_{5000ms}}{I_{50ms} - I_{5000ms}} \tag{15}$$

3.1.1 Incremental Capacity Analysis (ICA)

Incremental Capacity Analysis (ICA) is a method used to study the ageing and degradation mechanisms in an electrochemical system. The quasi-open circuit voltage can be obtained by discharging at a low C-rate. Figure 16 shows an example of an ICA curve of a Melasta cell at 100% state of health (SoH), where the dips in the graph represent changes in the structure of either one or both electrodes. This depends on the chemistry of the cell and varies for different battery cells. In order to understand and detect if the degradation occurs in one of the electrodes or both, a half cell of each electrode has to be made [8], [71], [72].
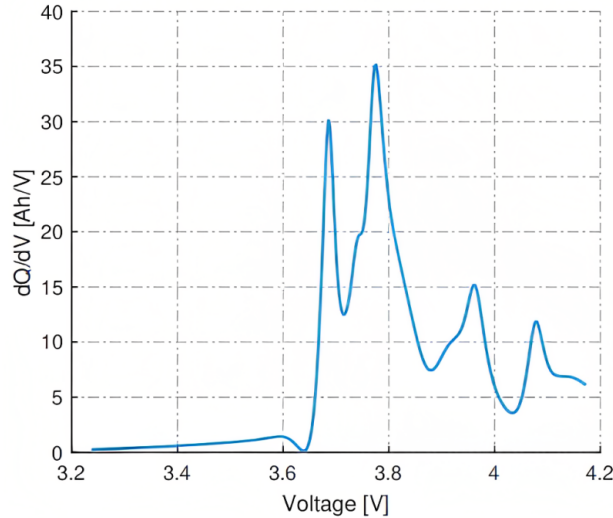
Figure 16: An Incremental Capacity Analysis (ICA) curve of the Melasta cell at 100% State of Health (SoH). Adapted from MacDonald and Trandem [8].

The dQ/dV can be calculated as follows:

$$\frac{dQ}{dV} \approx \frac{Q(t+1) - Q(t)}{V(t+1) - V(t)} \tag{16}$$

Here, Q is the total charge/discharge and V is the voltage at a time step t.

3.2 Cell Cooling Coefficient (CCC)

The Cell Cooling Coefficient (CCC) was used to determine the cooling potential of the cells. This was achieved with two different frequencies for the charge and discharge pulses: 0.25Hz and 1Hz and for different C-rates (3C, 3.5C, 4C and 4.5C). As mentioned in Section 2.3.2, the CCC is a physical property for measuring different cell surfaces and cell tabs. The different cooling methods, surface and tab cooling, ($CCC_{Surface}$ and CCC_{Tab}), are described below, and the constant values used in each calculation step are shown in Table 4 [3], [6], [7], [8], [73].

Table 4: Values used for calculating the heat generation from the Cell Cooling Coefficient (CCC) rig.

Variable	Value	Unit
$k_{aluminium\ 6082}$	180	$[W/mK]$
$A_{surf fin}$	$1.6 \cdot 10^{-4}$	$[m^2]$
$A_{tab\ busbar}$	$7.2 \cdot 10^{-5}$	$[m^2]$
Number of surface fins	4	[-]
Number of tab fins	2	[-]

3.2.1 Measuring the $\text{CCC}_{Surface}$

The $\text{CCC}_{Surface}$ measures how much heat the cell can dissipate by cooling one of the surface sides of the cell [7]. This coefficient is determined by first insulating the cell in an encapsulated styrofoam, as shown in Figure 17. The insulation minimizes heat losses during the measurements. The cell is mounted to the bottom part of the insulation with thermal paste. The aluminum plate on top of the rig (blue plate in Figure 18) was kept at a constant temperature using a water cooling block connected to cold water at 25℃. The thermocouples were then glued to the rig with thermal paste for measurement purposes, and the relative position was estimated using a digital caliper [3], [8].
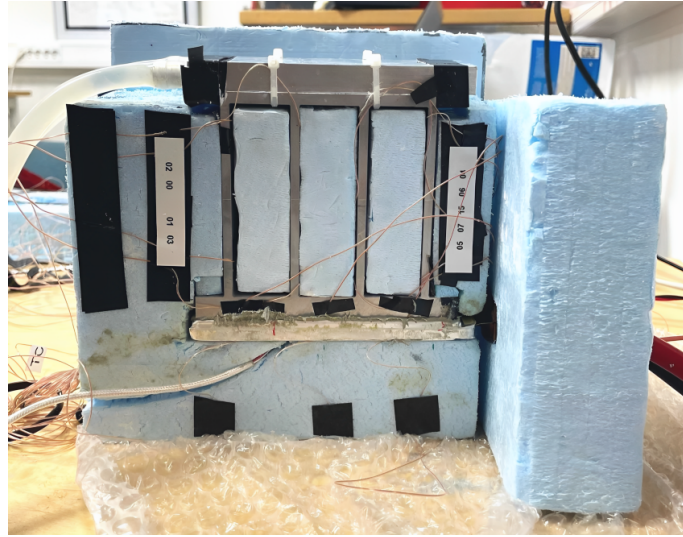
Figure 17: A picture of the $\text{CCC}_{Surface}$ setup where the cell is insulated in the bottom shell.

In addition, the ability of the cell to cool down was tested by cooling the surface and properly insulating the cell with bubble wrap to avoid interference from the ventilation in the room. An aluminum rig with four fins connected to thermocouples was used to cool the cell, as shown in Figure 18. Sixteen thermocouples (type K) were used, numbers 0 to 7 were used to measure the heat flux through the cell, and numbers 8 to 13 were used to measure the temperature gradient across the cell.

Number 14 was used as a control point to control the temperature of the tab, while number 15 was used to ensure that the heat flux through a half fin matched the heat flux through the whole fin [3], [8].
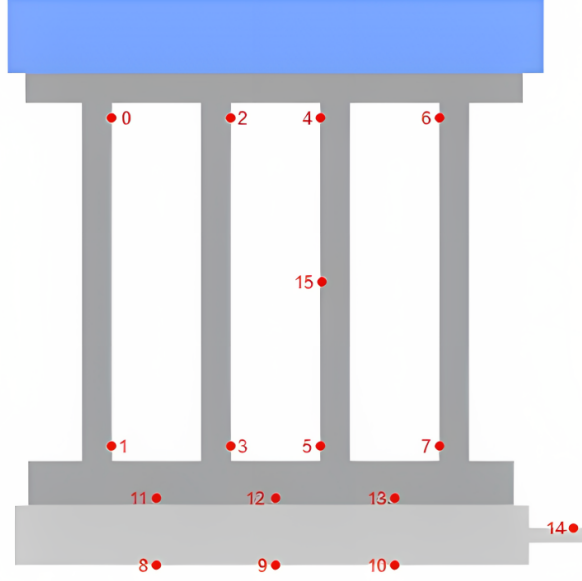
Figure 18: Sideview of the CCC$_{surface}$ rig with thermocouples.

3.2.1.1 Calculation of CCC$_{Surface}$

A Matlab code written by Christian Trandem and Colin MacDonald was employed to calculate the CCC values. As the thermal conductivity of the fins was known, the heat flux of each fin was calculated by using Equation 17. The total heat flux for the entire measurement was then calculated by using the following Equation 18 [3], [8].

$$\dot{Q}_{fin\ i} = \frac{k_{fin\ i}}{x_{fin\ i}} A_{fin\ i} \Delta T_{fin\ i} \tag{17}$$

$$\dot{Q}_{Surf} = \sum_{i=1}^{4} \dot{Q}_{fin\ i} \tag{18}$$

Here, $\dot{Q}_{fin\ i}$ refers to the sum of heat rejected from each fin, $k_{fin\ i}$ is the thermal conductivity of the fins, $A_{fin\ i}$ is the cross-sectional area of each fin, $x_{fin\ i}$ is the distance between the thermocouples on each fin measuring the temperatures, and $\Delta T_{fin\ i}$ is the temperature gradient in each fin measured by the thermocouples [3], [7].

The temperature difference on each side of the battery was calculated by using Equation 19. Figure 18 shows the temperature measuring points.

$$\Delta T_{Cell} = \frac{(T_8 + T_9 + T_{10})}{3} - \frac{(T_{11} + T_{12} + T_{13})}{3} \qquad (19)$$

Finally, the CCC$_{Surface}$ was determined by dividing the surface heat flux by the temperature difference of the cell as shown in Equation 20 [3].

$$CCC_{Surf} = \frac{\dot{Q}_{Surf}}{\Delta T_{Cell}} \qquad (20)$$

The following schedule was used for the CCC measurement:

- Constant Current Constant Voltage (CCCV) charge

- Discharge to 50% state of charge (SoC), C-rate

- Positive pulse, frequency, C-rate

- Negative pulse, frequency, C-rate

3.2.2 Measuring the CCC$_{Tab}$

In this method, the tabs are cooled at 12℃ by using busbars attached to the tabs. The end of the busbar (blue ends in Figure 19) was cooled using water cooling blocks, and the heat transfer through the tabs was determined using thermocouples (type K) glued to the busbars, as shown in Figure 19.
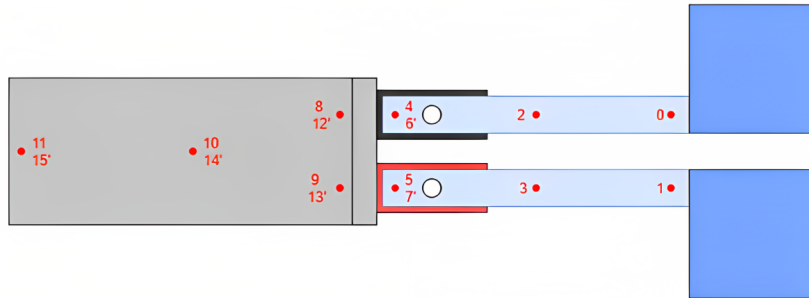
Figure 19: Top view of the CCC$_{tab}$ rig with thermocouples, where the numbers with a punctuation mark define the thermocouples under the cell.

The same schedule as for the CCC$_{Surface}$ was used to measure CCC$_{Tab}$. However, the difference between surface cooling and tab cooling is the component under cooling. The whole setup is shown in Figure 20 [3].
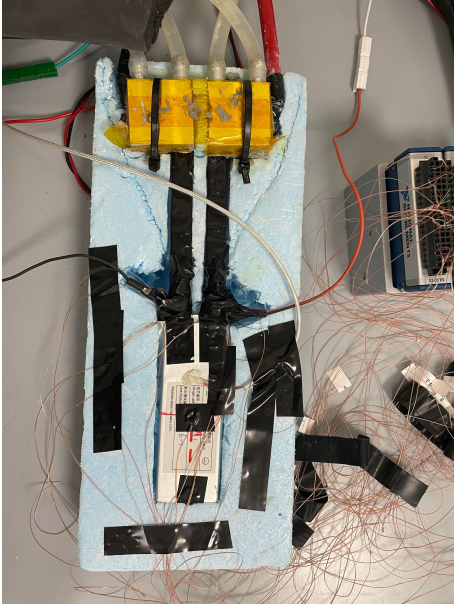
(a) Without insulation

(b) Setup ready for test run

Figure 20: Pictures of the CCC_{Tab} setup.

3.2.2.1 Calculation of CCC_{Tab}

These equations (Equation 21, 22, 24) were used to calculate the CCC for surface cooling and can also be used for measuring the CCC values for tab cooling. Equation 21 calculates the sum of the heat rejected from each tab, $\dot{Q}_{busbar\ i}$, where $k_{busbar\ i}$ is the thermal conductivity of the busbars, $A_{busbar\ i}$ is the cross-sectional area of each busbar and x_{busbar} is the distance between the negative or positive busbars [3], [8].

$$\dot{Q}_{Busbar\ i} = \frac{k_{busbar\ i}}{x_{busbar\ i}} A_{busbar\ i} \Delta T_{busbar\ i} \tag{21}$$

The only difference is that Equation 22 is calculated with two components [3], [8].

$$\dot{Q}_{Tab} = \sum_{i=1}^{2} \dot{Q}_{Busbar\ i} \tag{22}$$

The temperature difference for the cell is defined by the negative and positive busbars:

$$\Delta T_{\text{Cell}} = \frac{((T_{11} + T_{15})/2 - T_6) + ((T_{11} + T_{15})/2 - T_7)}{2} \tag{23}$$

Finally, the CCC_{tab} is calculated as follows:

$$CCC_{Tab} = \frac{\dot{Q}_{Tab}}{\Delta T_{Cell}} \tag{24}$$

3.3 Thermal conductivity

The thermal conductivity of the electrodes was measured using the thermal conductivity rig shown in Figure 21. A detailed description of this process and the rig can be found in the work of Burheim et al. [74]. As mentioned in Section 2.3.3, the purpose of these measurements is to investigate the heat transport inside the battery. This is essential to dimension and utilize cooling systems such as the CCC rigs mentioned earlier. This experimental setup used a constant heat flux to determine the thermal conductivity. The temperature of the steel rods above and below the sample was kept constant, and the heat flux across the samples was estimated from thermocouple measurements along the steel rods. Following this process, the material samples were placed between two 21 mm diameter steel rods, as shown in Figure 21. The 35℃ hot water was connected to the upper cylinder, while the lower cylinder was connected to 10℃ cold water [8], [48]. Moreover, the tip of each cylinder in contact with the samples is covered with aluminum, as it has higher thermal conductivity compared to steel. An isothermal region is created adjacent to the sample [3], [48].
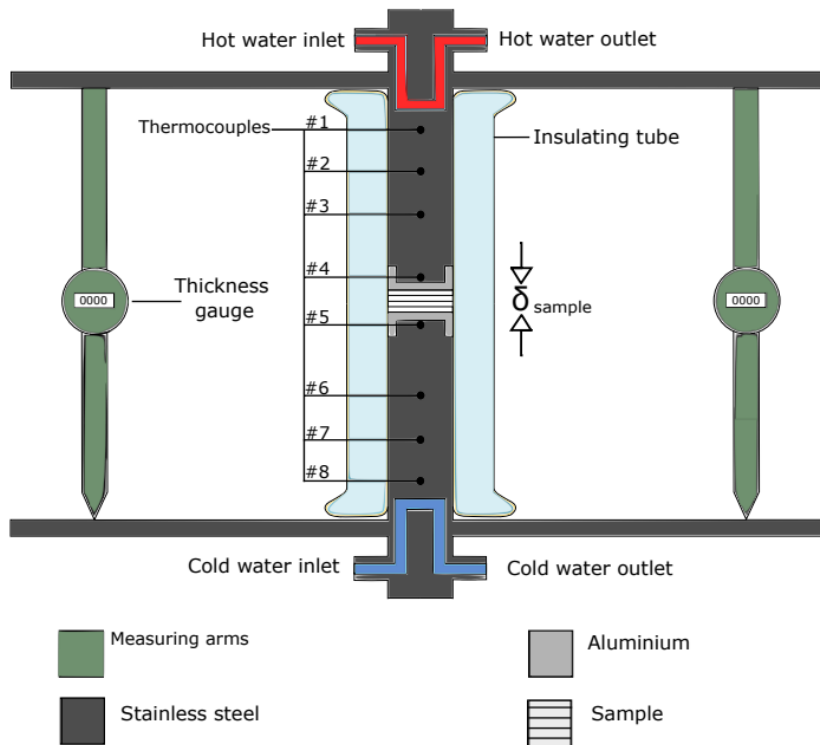

Figure 21: Rig used to measure thermal conductivity. Adapted from Richter et al. [53].

The temperature differences between points 1 and 3 and between points 6 and 8 from

Figure 21 were determined by using four thermocouples (type K) that were glued to each cylinder body with thermal paste. Based on these temperature measurements, two heat flux values were obtained: one through the upper cylinder and one through the lower cylinder. Comparing these two values ensured that the heat flowed in one direction. Two additional thermocouples were placed at points 4 and 5 on the aluminum section to measure the temperature drop across the sample. An insulation tube was placed around the cylinders while doing measurements to minimize heat loss [48].

To measure the variation in sample thickness due to applied pressure, two micrometers (type Mitutoyo Digimatic Indicator ID-C Series 543) were connected to the upper part of the rig and aligned with the cylinders. The applied pressure was provided by a pneumatic piston connected to the lower part of the rig. A regulator (type Rexroth R434000457) was utilized to regulate and control the pressure throughout the experiments. Thermocouples, micrometers, and the pressure regulator were connected to a computer to collect and analyze data. A LabView program was utilized to record the temperature and sample thickness data for each time and pressure step. [48].

3.3.1   Analyzed materials

As mentioned in Section 2.5, the battery cell studied in this work is Melasta No.: SLPBB042126 manufactured by Shenzen Melasta Battery Co. The cathode material used in this cell is a composition of Lithium Cobalt Oxide (LCO, $LiCOO_2$), while the anode material is graphite. For the planned measurements, the electrodes were taken from a battery cell at the beginning of life (BoL) after conducting the CCC measurements. In other words, these electrodes were extracted from a fully integrated battery cell that has undergone a formation cycle at the battery manufacturer. Following this process, the cell was stored in a warehouse until the electrodes were removed for thermal conductivity measurements. Both wet and dry electrodes were assessed in these measurements [48].

3.3.1.1   Electrode extraction

To measure the thermal conductivity of the Melasta cell, the cell was first fully discharged. Then, the cell was opened inside a glove box (LabMaster Pro Eco - MRBRAUN) with an argon atmosphere. Before being removed from the glove box, the harvested materials were cleaned with Dimethyl Carbonate (DMC) solvent. The cathode was washed for two minutes, while the anode was washed in two steps of 10 seconds each. After the cleaning process, the materials were desiccated for 48 hours before taking them out of the glove box [48].

3.3.1.2   Sample preparation

To prepare the samples, a hammer and a cutting tool with a specified diameter of 21± 0.1 were used. After the samples were cut, the thickness was estimated using a manual micrometer to ensure accurate measurements. The thickness measurements were taken at three different locations on each sample to ensure precision and accuracy. To record thickness measurements and other information such as the thickness measurements of each electrode, the sample stacking order, the material name, and the thermal conductivity of the steel rig [48], an Excel file was created. This file was used to organize the data of the sample preparation and the measurements.

3.3.2   Parameters

3.3.2.1   Dry measurements

To measure the thermal conductivity for the dry samples, the electrode samples were placed in the rig after being cut out. The pressure and time steps used in this measurement are presented in Table 5.

Table 5: Pressure and time steps for dry measurements [4].

Pressure	2 bar	2.9 bar	3.9 bar	4.8 bar	5.8 bar	6 bar	2 bar
Time	15 min	5 min	5 min	5 min	5 min	10 min	5 min

3.3.2.2   Wet measurements

In the wet measurements, the materials were soaked in Diethyl Carbonate (DEC), an electrolyte solvent, before measuring their thermal conductivity. The samples were soaked for 15 minutes prior to the measurement. To prevent the solvent from evaporating during testing, a tape was attached around the steel rods before using the insulation. The pressure and time steps used in this measurement are presented in Table 6 [48].

Table 6: Pressure and time steps for wet measurements [4].

Pressure	2 bar	2.9 bar	3.9 bar	4.8 bar	5.8 bar	6 bar	2 bar
Time	15 min	5 min	5 min	5 min	5 min	5 min	5 min

3.3.3   Calculations

The thermal conductivity and thermal resistance of the samples were calculated using a Matlab code written by Bern K. Holkenborg. This code uses Equation 25 to estimate the heat flux across the sample.

$$q_{sample} = \frac{q_{upper}}{q_{lower}}, q_{upper} = k_{steel}\frac{T_1 - T_3}{d_{1-3}}, q_{lower} = k_{steel}\frac{T_6 - T_8}{d_{6-8}} \qquad (25)$$

Then, the thermal resistance is calculated as follows:

$$R_{sample} = \frac{T_4 - T_5}{q_{sample}} = 2R_{contact\ res.} + \frac{\delta_{act.M.}}{k_{act.M.}} + \frac{\delta_{foil}}{k_{foil}} \qquad (26)$$

By stacking the samples in various thicknesses, as shown in Figure 22, the total thermal resistance, R_{sample}, and its contact resistance, $R_{contact\ resistance}$, were plotted as a function of the different component thicknesses. According to Richter et al., [53], the additional contact resistances such as the thermal contact resistance of the electrodes and current collectors can be neglected due to their high thermal conductivity. The thermal conductivity was then calculated by taking the inverse of the slope. The material samples were stacked in three or four different thicknesses to calculate the standard deviation [1], [3], [8], [48], [74].
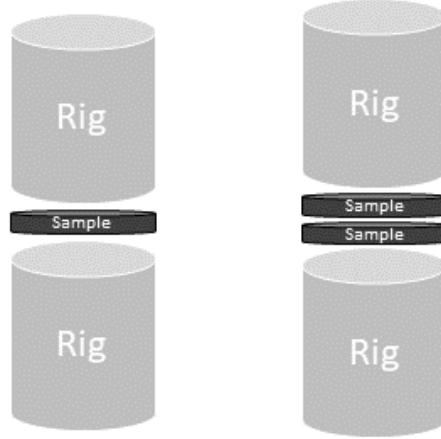
Figure 22: An illustration showing how the samples are stacked to obtain the thermal conductivity and the thermal resistance of the measured samples.

In the thermal conductivity measurement of both the anode and cathode materials, the measurements include the current collector and the active material of the active material on both sides of the current collector. To accurately determine the thermal conductivity of only the active material, it is necessary to subtract the current thickness of the current collectors from the total thickness of the electrode sample. By plotting the total thermal resistance against the adjusted thickness, a new line will be derived by performing a linear regression analysis on this plot [48].

3.4 Scanning Electron Microscope (SEM)

A scanning electron microscope (SEM) is a tool that uses a focused beam of electrons to generate images of the surface of a sample. A detailed explanation of this method is to be found in Section 2.3.5. SEM was employed to characterize the structure of the sample surfaces. The apparatus used was an FEI Apreo with Energy Dispersive X-ray (EDX) from the Nanolab at Norwegian University of Science and Technology (NTNU). Following this process, a working distance of approximately 10mm was used with increasing voltages between 3.00 to 5.00kV for all samples. The settings utilized for the SEM images are presented in Table 7.

Table 7: Imaging settings used for Scanning Electron Microscope (SEM) [68].

Parameters	Value	Unit
Mode	ETD	[-]
Working distance	≈ 10	[mm]
Current	0.10 - 0.40	[nA]
Voltage	3.00 - 5.00	[kV]

The anode and cathode materials were extracted from the same cell used for the other measurements. Specifically, a Melasta cell at BoL from the CCC measurements. Samples utilized in this tool were from the middle of the stack. To ensure that all contaminants were removed, the material was cleaned using DMC and then dried for 2 hours prior to the SEM, allowing full evaporation of DMC. The samples were prepared to fit in the SEM and during the analysis, the SEM chamber was filled with air so the samples were not exposed to the ambient atmosphere.

4 Results and Discussion

This chapter presents the results obtained from the experiments and provides a discussion of these findings. This includes cell characterization, Cell Cooling Coefficient (CCC) measurements, thermal conductivity measurements, and Scanning Electron Microscope (SEM) images.

4.1 Cell characterization

As mentioned in Section 3.1, the purpose of the characterization is to determine changes in the internal resistance and the battery capacity. Figure 23 shows the characterization test done for the battery in the surface cooling rig. A similar test was also done for the battery in the tab cooling rig. These characterization tests included different current rates, as presented in the schedule provided in Section 3.1. The plot from the surface cooling rig clearly indicates the normal operation of the battery. This aligns with the results from a similar test done by Christian Foyn in his master thesis [11].
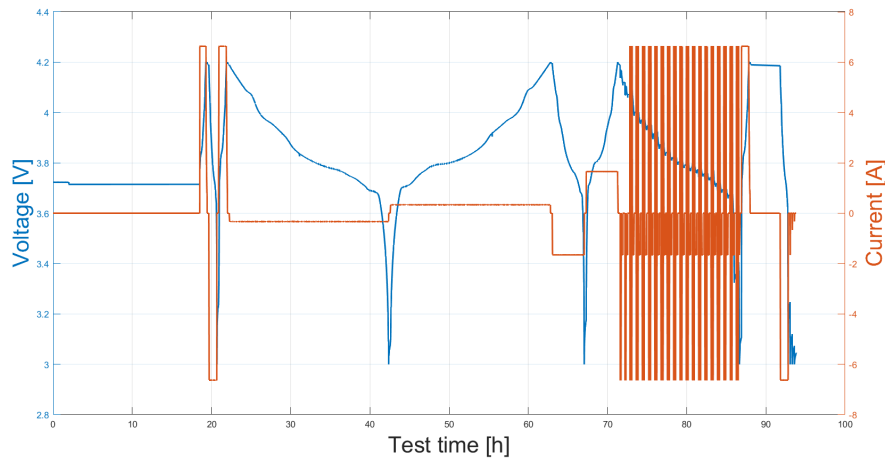
Figure 23: Plot of the voltage and current during the characterization test. The battery is charged and discharged at 1C, C/20 and C/4 followed by a hybrid pulse power characterization (HPPC) test.

From the characterization of the battery, the Incremental Capacity Analysis (ICA) curve was obtained as shown in Figure 24. This curve was plotted using Equation 16 and cycles with C/20. The plot of the dQ/dV curve is similar to the plot of the ICA curve by Trandem and MacDonald shown in Section 3.1.1. It confirms that the cell is at 100% state of health (SoH) [8] and functions properly with no indications of unrealistic electrochemical behavior, capacity fade or degradation of the battery.

Figure 24: Incremental Capacity Analysis (ICA) plot of the Melasta cell at 100% State of Health (SoH).

4.2 Cell Cooling Coefficient (CCC)

As explained in Section 3.2, the Cell Cooling Coefficients (CCCs) were characterized for different frequencies and C-rates to investigate the heat generation within the cells and to determine how the cooling potential changes with increasing frequency. In the following figures, the blue areas represent the current pulses, while the rest periods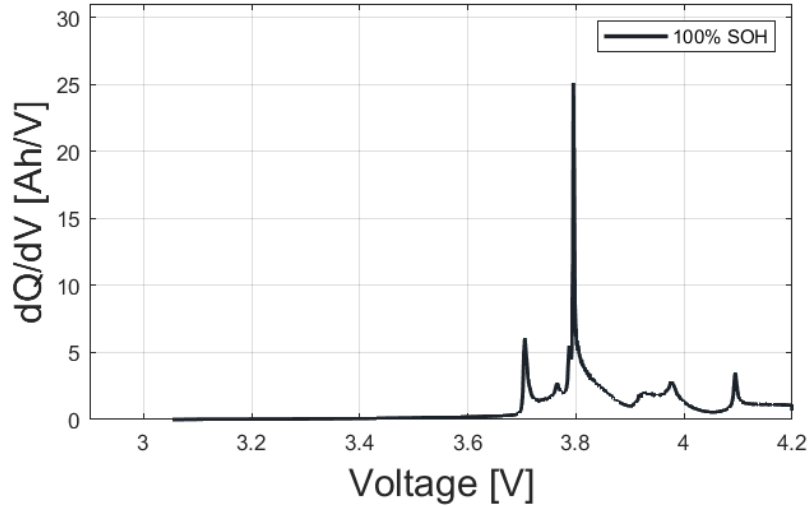 are not highlighted. This pulse rate was held constant for 3.6 hours to assure stable temperature measurements. Both measurements were performed with a one-hour interval rest period between each CCC characterization test.

4.2.1 $CCC_{Surface}$

Figure 25 shows the surface cooling measurements at 0.25Hz for four different C-rates (3C, 3.5C, 4C and 4.5C) studied in this work. During the rest periods, the temperature across the cell reaches zero and the CCC approaches infinity, which can be confirmed by Equation 20. Therefore, data points where δT is less than 1℃ and where the CCC values are unrealistic or considered noise are excluded from the analysis. The figure indicates that the CCC reaches its most stable state when the current is at its highest, at 4.5C. This correlates with the results of Spitthoff et al. [4], who did a comparable CCC characterization test. The study explains that this is due to a larger denominator in Equation 10. In addition, the $CCC_{Surface}$ value of approximately 0.8W/K corresponds with the values reported in the work of Spitthoff et al. [4].

Figure 25: Plots of CCC$_{Surface}$ measurements done for the Melasta cell at 100% State of Health (SoH) for different C-rates at 0.25Hz, where a) 3C, b) 3.5C, c) 4C and d) 4.5C. The line graph in the highlighted blue area represents the current pulses at a given frequency.

Figure 26 shows the surface cooling measurements at 1Hz for four different C-rates (3C, 3.5C, 4C and 4.5C), which was also studied in this work. The $CCC_{Surface}$ value, in this case, is approximately 0.8 W/K. This is similar to the value as for the measurement at 0.25Hz.
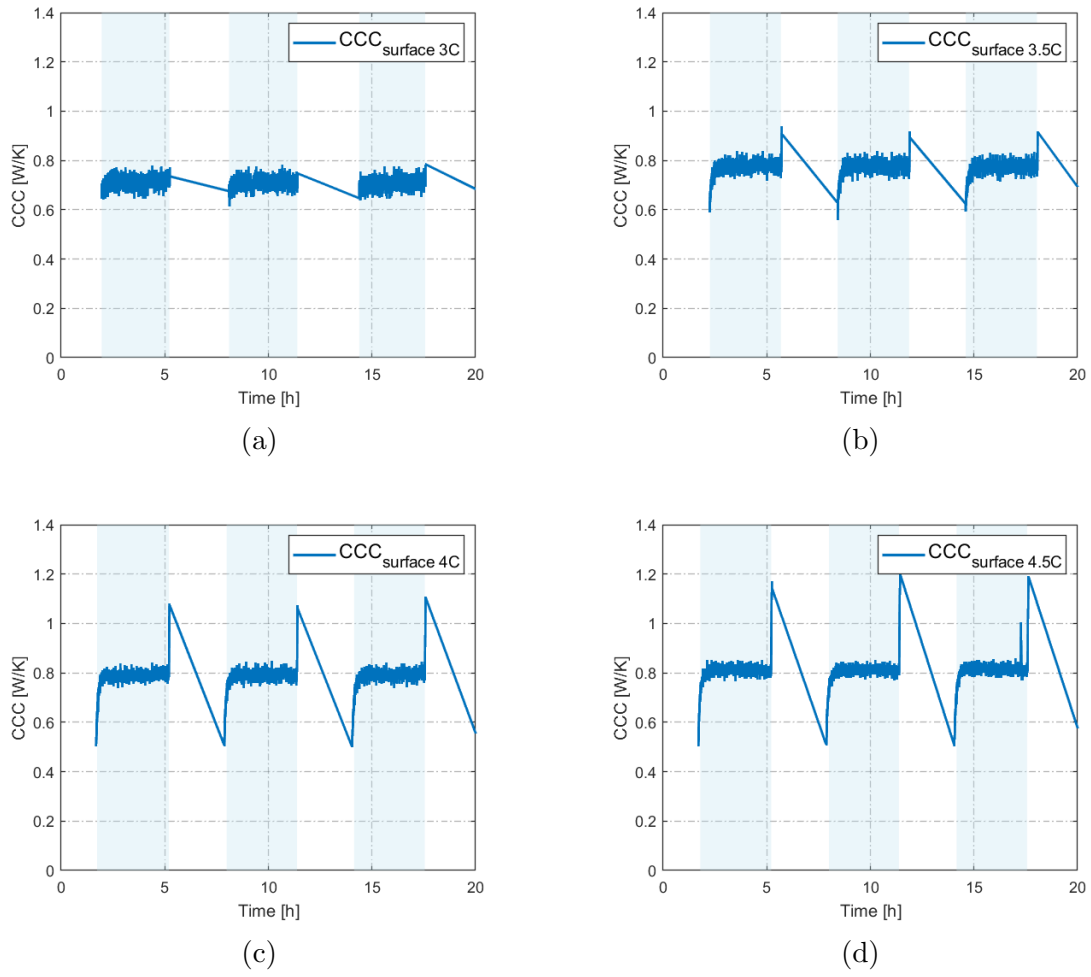

Figure 26: Plots of $CCC_{Surface}$ measurements done for the Melasta cell at 100% State of Health (SoH) for different C-rates at 1Hz, where a) 3C, b) 3.5C, c) 4C and d) 4.5C. The line graph in the highlighted blue area represents the current pulses at a given frequency.

When comparing the CCC values for both scenarios, the frequency is changed. Even though there is a slight increase in heat generation, it does not necessarily affect all surface cooling systems. The change in frequency in the range of 0.25Hz to 1Hz does not seem to affect the cooling system, which means that the frequency change does not result in an increase in the cooling potential. It is also worth mentioning that the correlation between the frequency and $CCC_{Surface}$ varies for different cell specifications and is dependent on the cell design and the cooling system.

4.2.2 CCC_{Tab}

After several measurements in an attempt to obtain stable temperatures, the presented data of the CCC_{Tab} are the most reliable. Figures 27 and 28 show the cooling potential of the tabs at frequencies of 0.25Hz and 1Hz. These plots show fluctuations in the temperature measurements, confirming the inconsistent and unstable temperature readings. Throughout the experimental setup and data collection, the measurements were affected by the overly sensitive thermocouples. As a result, the measured temperatures fluctuated in the range between 17℃ and 3100℃, which is considered unrealistic and unpredictable. This explains the high CCC_{Tab} values for all the measurements. However, the plots for the frequency of 1Hz indicate more peaks, which is due to a combination of faster current pulses that make it harder for the CCC_{Tab} to reach a steady state.
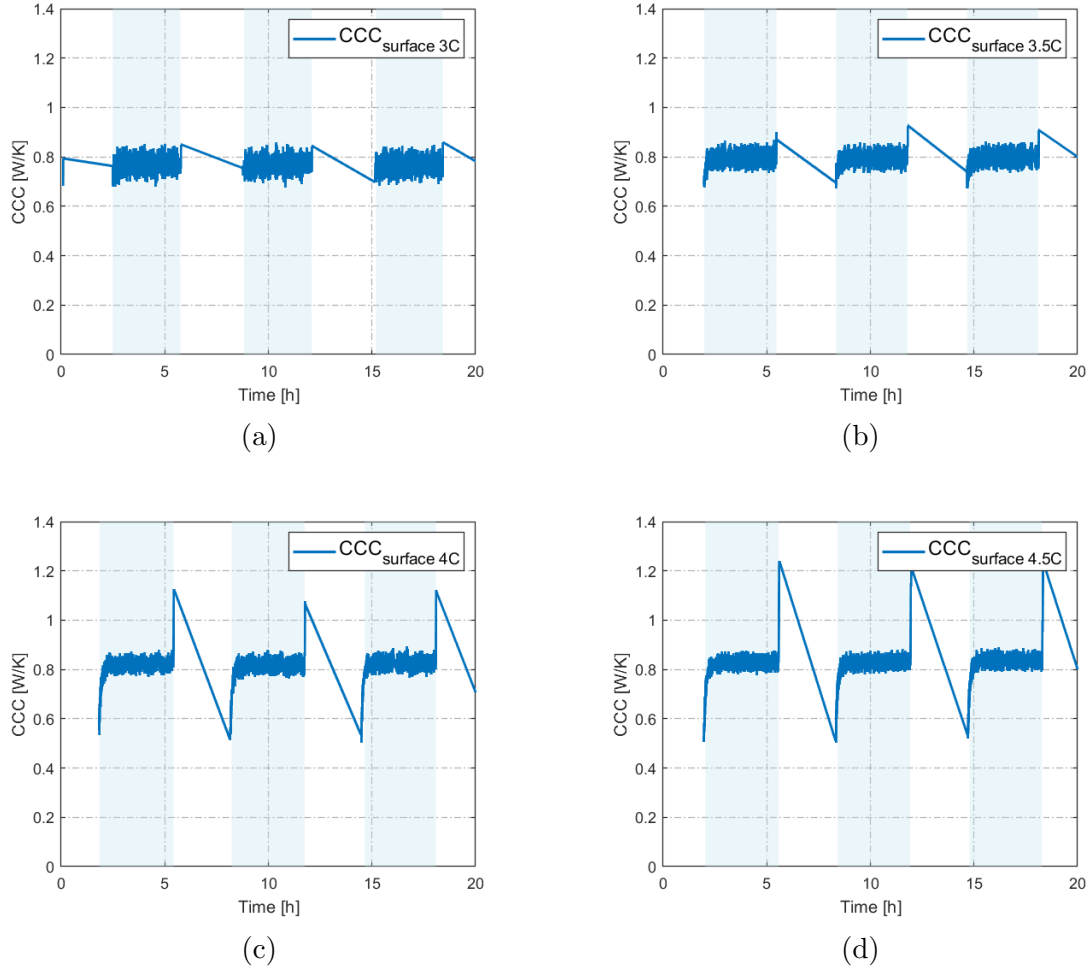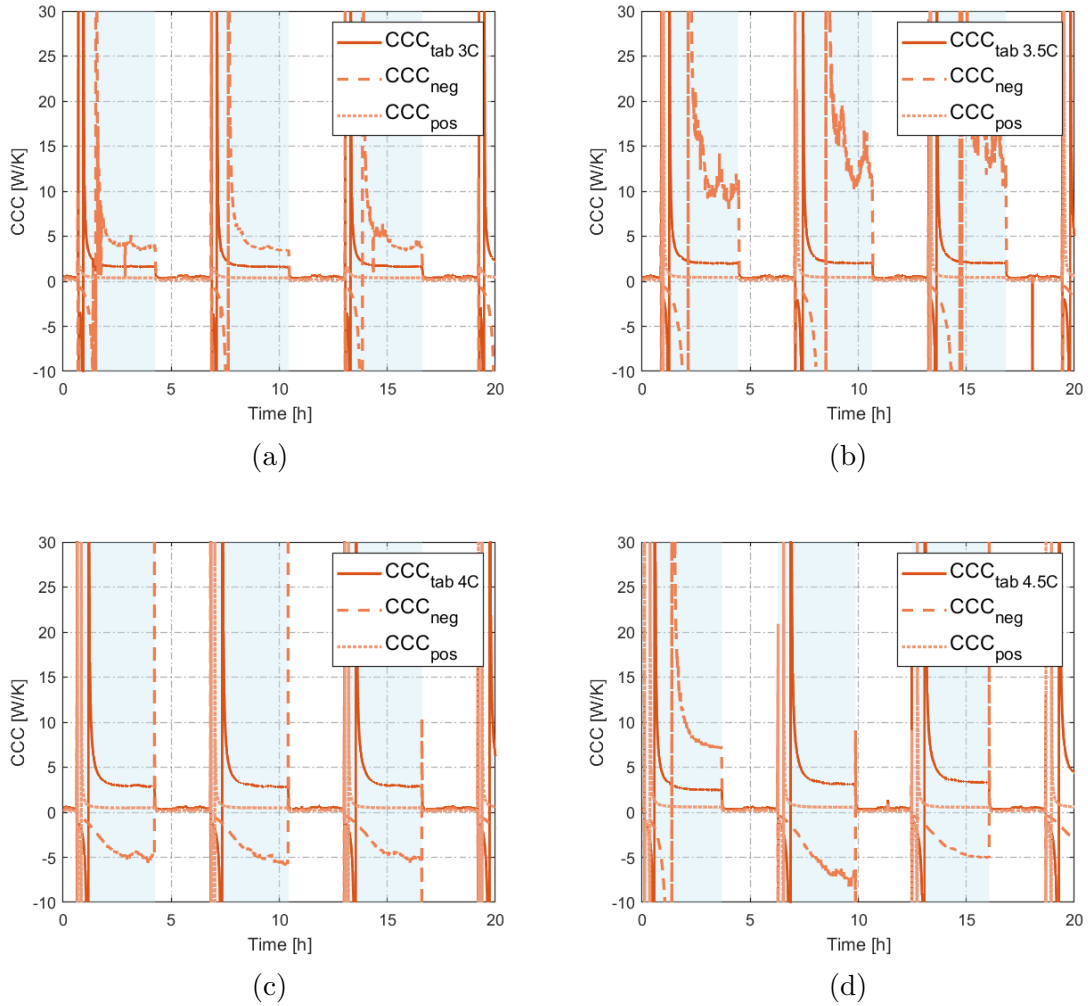

Figure 27: Plots of CCC_{Tab} measurements done for the Melasta cell at 100% State of Health (SoH) for different C-rates at 0.25Hz, where a) 3C, b) 3.5C, c) 4C and d) 4.5C. The red solid line in the highlighted blue area represents the current pulses at a given frequency.
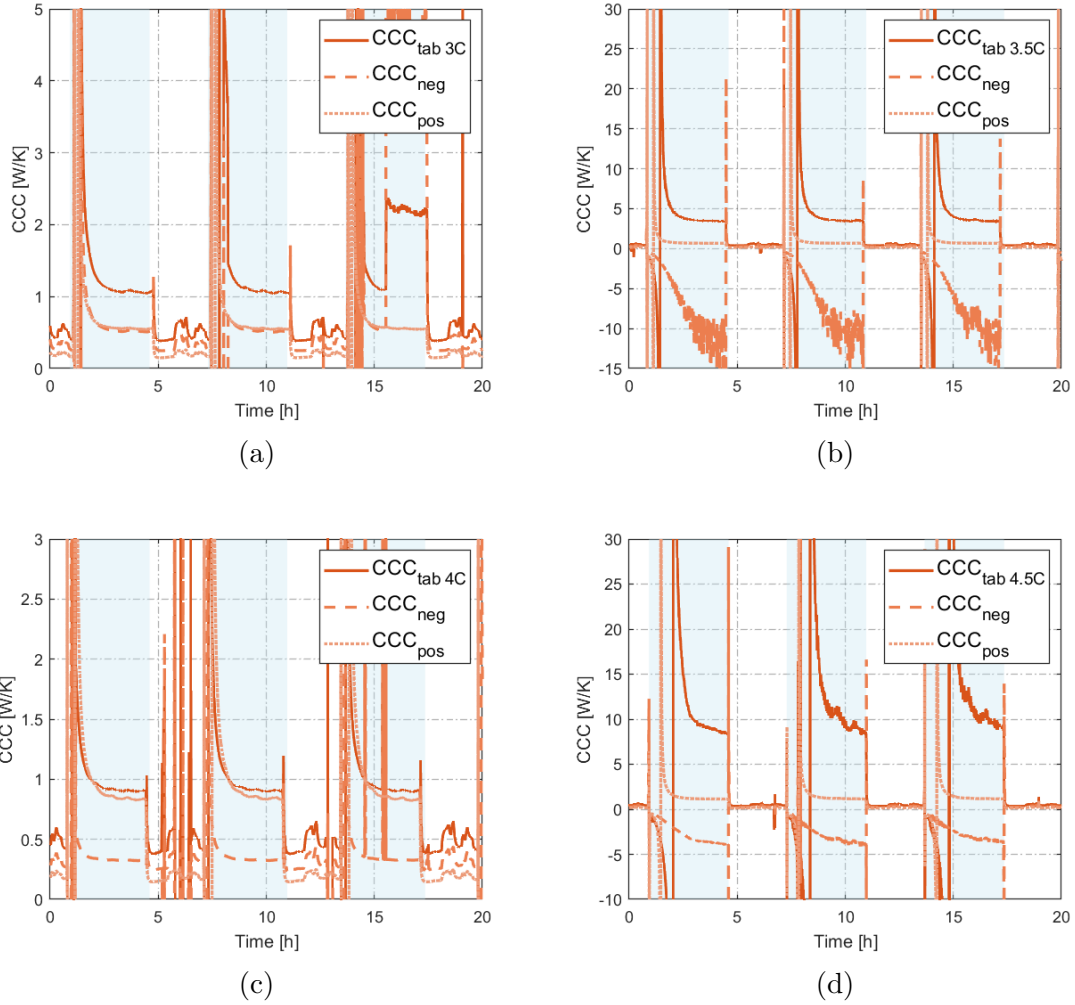
Figure 28: Plots of CCC_{Tab} measurements done for the Melasta cell at 100% State of Health (SoH) for different C-rates at 1Hz, where a) 3C, b) 3.5C, c) 4C and d) 4.5C. The red solid line in the highlighted blue area represents the current pulses at a given frequency.

Given the problems with thermocouples, it is necessary to look critically at the results of these graphs. The unstable temperature measurements and heat losses through other pathways certainly affect the accuracy and reliability of the cooling system discussed.

4.2.3   Heat generation

As discussed in Section 2.3.1, heat is generated due to electrochemical reactions, side reactions, irreversible processes and changes in the internal resistance. Figure 29 shows the heat generation for the $CCC_{Surface}$ for 0.25Hz and 1Hz. In this case, increasing the frequency for the current pulses from 0.25Hz to 1Hz does not appear to have a significant impact on heat generation.
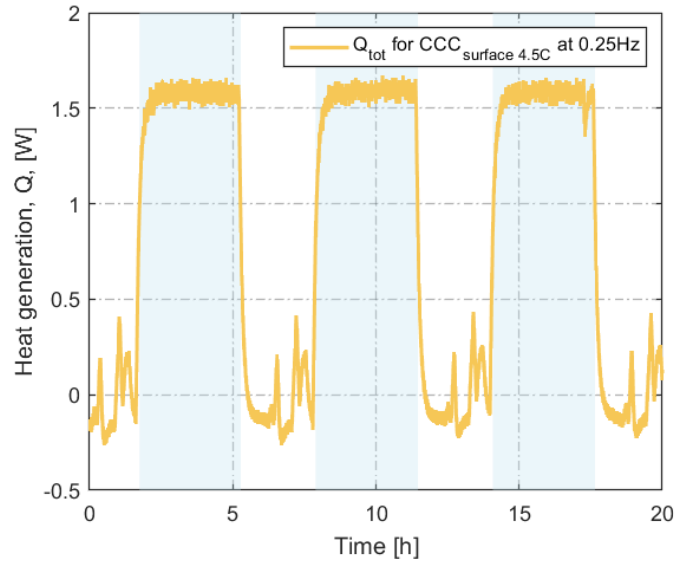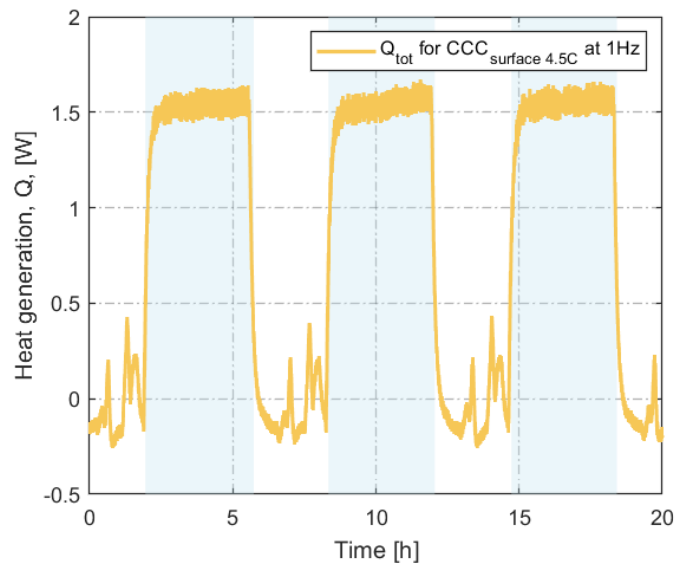
Figure 29: Heat generation for the CCC$_{Surface}$ at a) 0.25Hz and b) 1Hz.

4.2.4 Independence of C-rate

Trandem and MacDonald [8] concluded in their thesis that the C-rate has no significant impact on the CCC. This relationship is also confirmed in this thesis, as presented in Figure 27 and 26. The plots clearly indicate that increasing the C-rate does not lead to any remarkable changes.

4.3 Visual inspection of the battery cell

As mentioned in Section 3.3, a Melasta cell was opened after the CCC measurements to extract electrodes for Scanning Electron Microscope (SEM) images and thermal conductivity measurements. Detailed information such as the number of layers and thickness of the components was obtained from this procedure. The first and last layer was coated with an anode electrode material. This cell had 42 anode layers and 41 cathode layers. The uneven amount of electrodes was due to the current collectors that had electrode material on both sides and the reason for the extra anode is that graphite is lighter than Lithium Cobalt Oxide (LCO). Figure 30 shows the process of separating the electrode layers from each other.
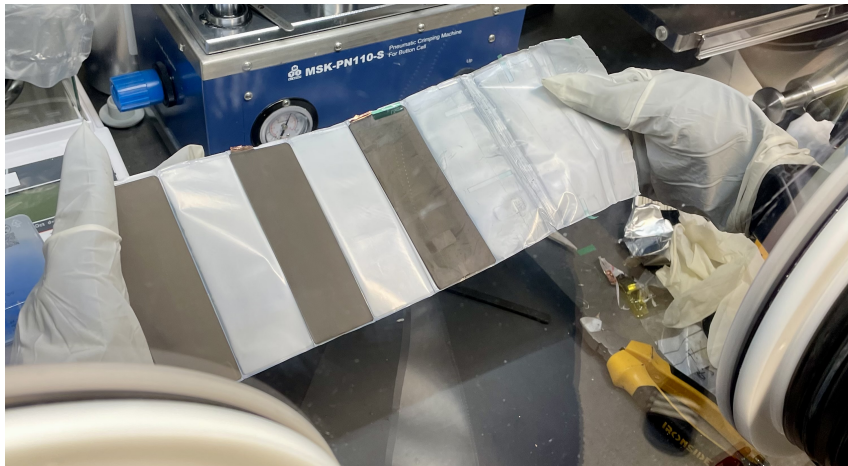
Figure 30: Separating the cell layers from each other
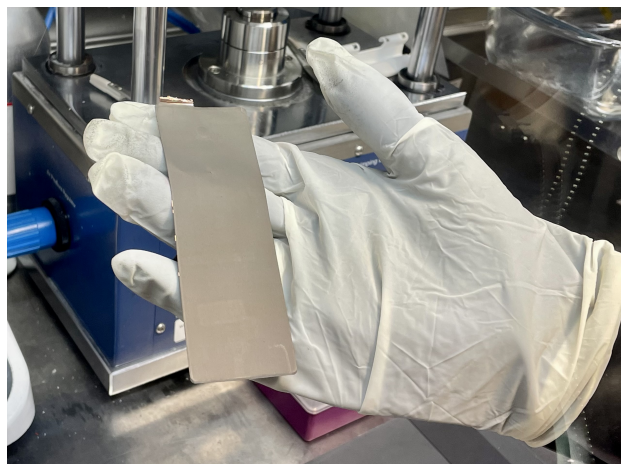
Figure 31: Anode material (graphite) from the Melasta cell with Copper (Cu) current collector.

Figure 32: Cathode material (Lithium Cobalt Oxide, LCO) from the Melasta cell with Aluminum (Al) current collector.

The Melasta cell had a separator, which was folded around the battery and secured with tape. It was Z-folded around the electrodes, so that the separator was one continuous sheet wrapped between the electrode layers. Figures 31 and 32 show the active materials of the anode and cathode layers. There were no observed changes in the structures of the active material. Furthermore, there were no signs of lithium plating, Solid Electrolyte Interphase (SEI) layer formation, or other ageing or degradation mechanism mentioned in Section 2.4. This process of opening the cell confirms that the Melasta cell operated normally during the CCC measurements and was in good condition without any significant changes affecting its performance.

4.4 Thermal conductivity

The thermal conductivity measurements of the battery were conducted following the experimental setup described in Section 3.3, and the presented data were obtained by using the formulas and the Matlab code in Section 3.3.3. The purpose of these measurements was to gain insight into the heat transport inside the cell as explained in Section 2.3.3. In Table 8, the collected data from the measurements are presented.

Table 8: Thermal conductivity of the measured material from the Melasta cell. The errors presented are the double standard deviation resulting from the linear regression.

| P [bar]	K_{Anode}^{dry} [W/mK]	$K_{Cathode}^{dry}$ [W/mK]	K_{Anode}^{wet} [W/mK]	$K_{Cathode}^{wet}$ [W/mK]
2.0	0.5256 ± 0.15	0.6494 ± 0.35	1.4712 ± 0.08	1.1518 ± 0.04
2.9	0.5649 ± 0.15	0.6863 ± 0.38	1.6381 ± 0.08	1.2023 ± 0.07
3.9	0.6119 ± 0.14	0.7241 ± 0.37	1.7431 ± 0.05	1.2574 ± 0.18
4.8	0.6549 ± 0.13	0.7533 ± 0.38	1.8570 ± 0.07	1.2911 ± 0.23
5.8	0.6883 ± 0.12	0.7727 ± 0.36	1.8683 ± 0.09	1.3658 ± 0.33
6.0	0.7152 ± 0.13	0.7965 ± 0.38	1.9114 ± 0.24	1.3310 ± 0.16

The measured thermal conductivity of the dry anode from the Melasta cell showed an increase of 36% from 0.5256W/mK to 0.7152W/mK when the applied pressure increased from 2 bar to 6 bar. Similarly, there was an increase in the dry cathode at a lower rate. The thermal conductivity of the cathode rose by 23% from 0.6494W/mK to 0.7965W/mK with the same applied pressure.

For the wet measurements, the soaked samples showed a noticeably higher thermal conductivity. The thermal conductivity measured for the wet anode showed a significant increase of 30% from 1.4712W/mK to 1.9114W/mK when the applied pressure increased from 2 bar to 6 bar. Correspondingly, the thermal conductivity of the wet cathode showed an increase at a relatively low rate. The thermal conductivity measured for the wet cathode of the Melasta cell showed an increase of 16% from 1.1518W/mK to 1.3310W/mK for the same pressure steps.

The values obtained correspond with the reported range of values by Spitthoff et al. [4]. However, it is essential to note that there was a systematic error of 5% because of the experimental setup and calibration process. The reason for this significant observation of increased thermal conductivity between the dry and the wet electrodes is due to the electrolyte. As illustrated in Figure 33, this observation points out the impact of electrolyte.
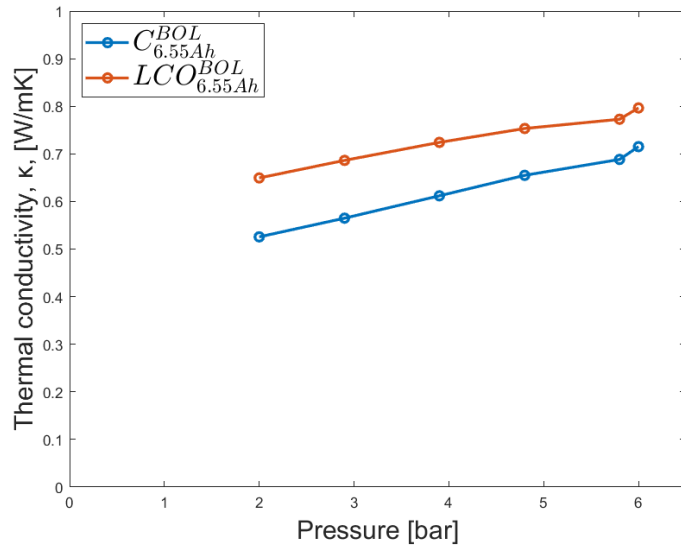
(a) Dry
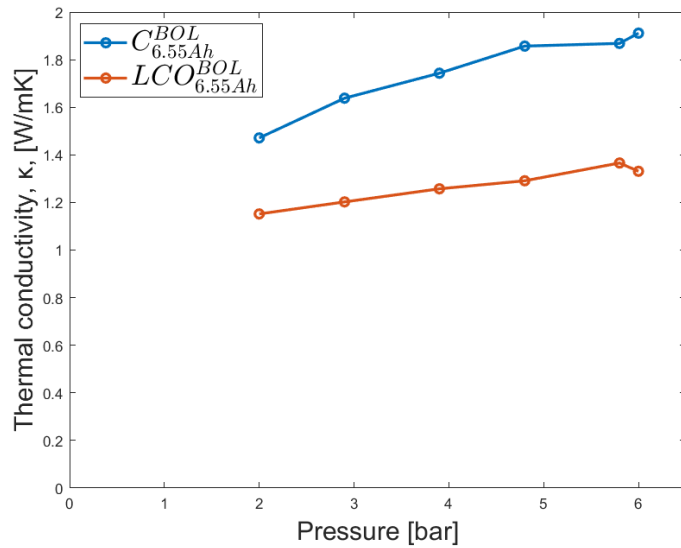
(b) Soaked

Figure 33: Thermal conductivity of electrode material from the Melasta cell at beginning of life (BoL).

Similar measurements are done by Spitthoff et al. who explain that the electrolyte improves the thermal conductivity, because it fills the voids in the pore structure. According to their findings, this enables heat transmission, even though the thermal conductivity of the electrolyte is low (between 0.45 and 0.6 W/mK) [4]. These results confirm that the electrolyte plays an important role in increasing the overall thermal conductivity of the battery.

4.5　Scanning Electron Microscope (SEM)

SEM images presented in this section were taken using the setup described in Section 3.4 to capture high-resolution images of the battery cell used in the CCC, and thermal conductivity measurements. The purpose of these images was to ensure that the cell operated normally and to investigate any potential structural changes which can influence the heat transfer and the cooling efficiency.

In the figure presented, the left side includes three images of the LCO cathode with different magnifications. These illustrate the microstructure and surface features of the cathode layer. It is clear to see that the active mass is not a single mass but includes countless electrode particles. On the right side of the figure, three images of the graphite are presented. These images indicate the structure and surface features of the material which is used as the anode in the Melasta cell. It is clear to see a layered structure with graphite flakes. Similar SEM images of the anode have been taken by Siburian et al. who confirm that graphite has wide and thick particles [75].
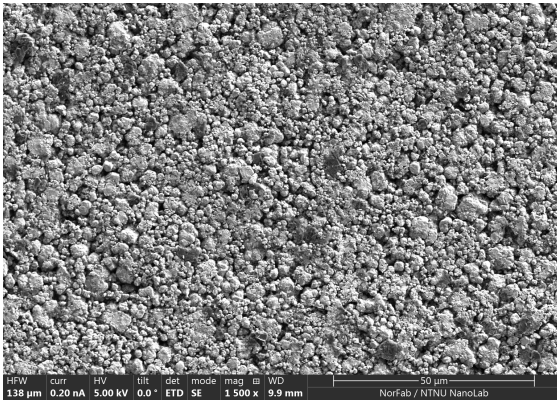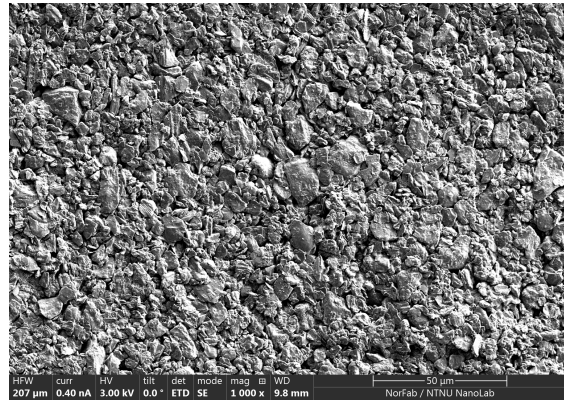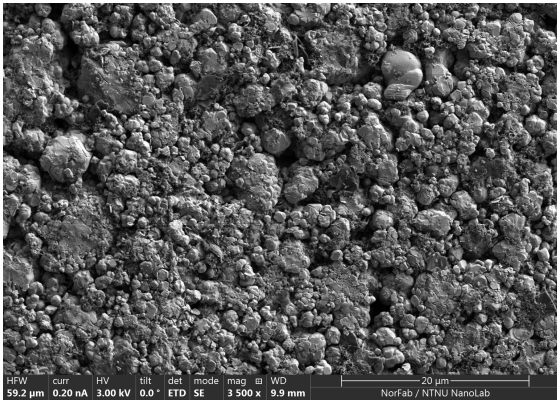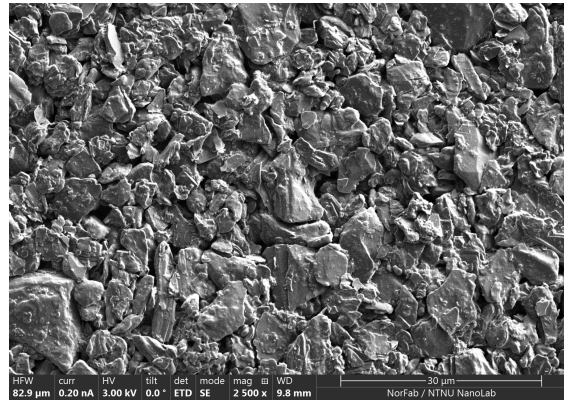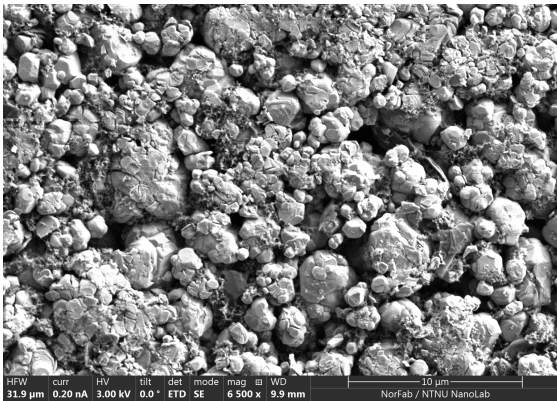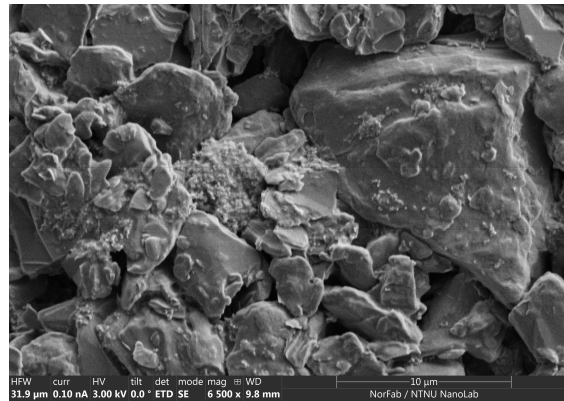
Figure 34: Scanning Electron Microscope (SEM) images of the graphite anode (b, d, f) and Lithium Cobalt Oxide (LCO) cathode (a, c, e) at beginning of life (BoL) from the Melasta cell with different magnifications.

When studying the images, there are no indications of lithium plating, SEI layer formation or other ageing or degradation mechanisms mentioned in Section 2.4. This confirms that the cell is a Lithium-ion battery (LiB) at beginning of life (BoL). In addition, these images provide a deeper understanding of the thermal properties in the battery. The images allow one to see the structural differences such as the

surface roughness, particle shape and sizes and other features which can affect the electrochemical reactions in the battery. Each particle of both electrodes contributes to the electrochemical activities and the overall performance of the battery.

5 Conclusion

This work assessed the cooling potential in Lithium-ion batteries (LiBs), which is critical as the temperature is an important factor in expanding the lifespan of the batteries. To solve this problem, a proper cooling system and an optimized design of the thermal management system (TMS) are required. By maintaining the heat generated in the battery during cycling, the cooling systems benefit the battery by regulating the temperature within a safe range, preventing overheating and in extreme cases fire or explosions. In the context of this, the thermal conductivity of electrodes from the Melasta cell at the beginning of life (BoL), Scanning Electron Microscope (SEM) images, and the overall Cell Cooling Coefficient (CCC) were measured for different frequencies.

When looking at the CCC method, the data revealed that there were no increase in $CCC_{Surface}$ values when the frequency range increased from 0.25Hz to 1Hz. The CCC value was approximately 0.8W/K for both cases. The cooling potential of the system remained unchanged for the studied frequency range. There were no definitive conclusions made for the CCC_{Tab} measurements due to inconsistent temperature readings from the experimental setup.

For the thermal conductivity measurements, the data gave detailed insight into the heat transport inside the battery. This indicated observable changes in thermal conductivity for both dry and wet electrodes at different applied pressures. The measurements performed on the Melasta cell highlighted the influence of electrolyte, showing an increase in thermal conductivity for the anode and cathode materials.

The SEM images confirmed that the cell functioned properly during the CCC measurements and contributed to the investigation of the thermal properties and electrochemical activities. There were no indications of lithium plating, SEI layer formation, and other ageing or degradation mechanisms typically affecting the battery performance.

In conclusion, the CCC measurements, thermal conductivity measurements, and SEM images gave important information about the functioning of the Melasta cell, heat transfer, and overall performance. However, it is proved that the CCC rigs are not properly functioning, which limits the accuracy and reliability of the obtained CCC data. Further improvements and investigation on the CCC rigs are needed to achieve accurate information on the cooling capability of LiBs.

6 Further work

The cooling potentials and thermal properties discussed in this thesis are limited due to restrictions of the surface cooling and tab cooling rigs. Additionally, the software used only allowed a few data points. Therefore, some improvements are required. A more in-depth study of the cooling potential with more data points and frequencies outside the studied range might be interesting for more accurate estimates and analysis.

Another interesting parameter to investigate is the impact of the cooling temperature on the heat generation. The temperature plays an essential role in the thermal properties and behavior of the system under various circumstances. This investigation will give valuable insight into which electrochemical processes and heat sources that dominate at high temperatures. This knowledge will help to optimize the cooling systems and build better thermal management systems (TMSs).

In addition, a State of Charge (SoC) study to explore how different SoC values influence heat generation will be beneficial. This research will give in-depth information about dominating heat generation processes within the cells and find thermal management requirements needed to develop efficient cooling systems.

If the same method is to be used in the future, a development of the rig is required. A lot of time was spent troubleshooting the rigs with the thermocouples. Optimization of the surface and tab cooling rigs by redesigning the entire setup could benefit further research as well as considering the use of different temperature sensors and insulation materials.

Bibliography

[1] J. J. Lamb and B. G. Pollet, Eds., *Micro-Optics and Energy: Sensors for Energy Devices*, en. Cham: Springer International Publishing, 2020, ISBN: 978-3-030-43675-9 978-3-030-43676-6. DOI: 10.1007/978-3-030-43676-6.

[2] O. S. Burheim, 'Chapter 7 - Secondary Batteries', en, in *Engineering Energy Storage*, O. S. Burheim, Ed., Academic Press, Jan. 2017, pp. 111–145, ISBN: 978-0-12-814100-7. DOI: 10.1016/B978-0-12-814100-7.00007-9.

[3] S. Athisayamohan, *Measuring the cooling capability of Lithium-ion batteries*, Dec. 2022.

[4] L. Spitthoff, M. S. Wahl, P. J. S. Vie and O. S. Burheim, 'Thermal transport in lithium-ion batteries: The effect of degradation', en, *Journal of Power Sources*, vol. 577, p. 233 149, Sep. 2023, ISSN: 0378-7753. DOI: 10.1016/j.jpowsour.2023.233149.

[5] *Electric Vehicles to Drive Massive Battery Demand: BNEF Chart*, en. [Online]. Available: https://news.bloomberglaw.com/environment-and-energy/electric-vehicles-to-drive-massive-battery-demand-bnef-chart.

[6] A. Hales, L. B. Diaz, M. W. Marzook, Y. Zhao, Y. Patel and G. Offer, 'The Cell Cooling Coefficient: A Standard to Define Heat Rejection from Lithium-Ion Batteries', en, *Journal of The Electrochemical Society*, vol. 166, no. 12, A2383–A2395, 2019, ISSN: 0013-4651, 1945-7111. DOI: 10.1149/2.0191912jes.

[7] L. B. Diaz, A. Hales, M. W. Marzook, Y. Patel and G. Offer, 'Measuring Irreversible Heat Generation in Lithium-Ion Batteries: An Experimental Methodology', en, *Journal of The Electrochemical Society*, vol. 169, no. 3, p. 030 523, Mar. 2022, ISSN: 0013-4651, 1945-7111. DOI: 10.1149/1945-7111/ac5ada.

[8] C. R. MacDonald and C. H. Trandem, 'Impact of Cooling Methods on Ageing in Lithium-ion Battery Cells', eng, Accepted: 2021-10-20T17:28:45Z, M.S. thesis, NTNU, 2021. [Online]. Available: https://ntnuopen.ntnu.no/ntnu-xmlui/handle/11250/2824272.

[9] N. Faezaa, S. Toha, N. Azubir, N. Ishak, M. K. Hassan and B. S. KSM Kader Ibrahim, 'Simplified Heat Generation Model for Lithium ion battery used in Electric Vehicle', *IOP Conference Series: Materials Science and Engineering*, vol. 53, p. 012 014, Dec. 2013. DOI: 10.1088/1757-899X/53/1/012014.

[10] *Anode Material - an overview — ScienceDirect Topics*. [Online]. Available: https://www.sciencedirect.com/topics/materials-science/anode-material.

[11] C. B. Foyn, 'Temperature measurement in lithium-ion batteries using FBG', eng, Accepted: 2022-09-22T17:19:56Z, M.S. thesis, NTNU, 2022. [Online]. Available: https://ntnuopen.ntnu.no/ntnu-xmlui/handle/11250/3020766.

[12] H. Zhang, Y. Yang, D. Ren, L. Wang and X. He, 'Graphite as anode materials: Fundamental mechanism, recent progress and advances', en, *Energy Storage Materials*, vol. 36, pp. 147–170, Apr. 2021, ISSN: 2405-8297. DOI: 10.1016/j.ensm.2020.12.027.

[13] N. Nitta, F. Wu, J. T. Lee and G. Yushin, 'Li-ion battery materials: Present and future', en, *Materials Today*, vol. 18, no. 5, pp. 252–264, Jun. 2015, ISSN: 1369-7021. DOI: 10.1016/j.mattod.2014.10.040.

[14] P. U. Nzereogu, A. D. Omah, F. I. Ezema, E. I. Iwuoha and A. C. Nwanya, 'Anode materials for lithium-ion batteries: A review', en, *Applied Surface Science Advances*, vol. 9, p. 100 233, Jun. 2022, ISSN: 2666-5239. DOI: 10.1016/j.apsadv.2022.100233.

[15] Y. Lu, L. Yu and X. W. (Lou, 'Nanostructured Conversion-type Anode Materials for Advanced Lithium-Ion Batteries', en, *Chem*, vol. 4, no. 5, pp. 972–996, May 2018, ISSN: 2451-9294. DOI: 10.1016/j.chempr.2018.01.003.

[16] J. Garche, E. Karden, P. Moseley and D. Rand, *Lead-Acid Batteries for Future Automobiles*. Mar. 2017, Journal Abbreviation: Lead-Acid Batteries for Future Automobiles Pages: 674 Publication Title: Lead-Acid Batteries for Future Automobiles.

[17] Z. Liu, Q. Yu, Y. Zhao *et al.*, 'Silicon oxides: A promising family of anode materials for lithium-ion batteries', en, *Chemical Society Reviews*, vol. 48, no. 1, pp. 285–309, 2019, Publisher: Royal Society of Chemistry. DOI: 10.1039/C8CS00441B.

[18] N. P. Wagner, A. Tron, J. R. Tolchard, G. Noia and M. P. Bellmann, 'Silicon anodes for lithium-ion batteries produced from recovered kerf powders', en, *Journal of Power Sources*, vol. 414, pp. 486–494, Feb. 2019, ISSN: 0378-7753. DOI: 10.1016/j.jpowsour.2019.01.035.

[19] C.-M. Park, J.-H. Kim, H. Kim and H.-J. Sohn, 'Li-alloy based anode materials for Li secondary batteries', en, *Chemical Society Reviews*, vol. 39, no. 8, pp. 3115–3141, Jul. 2010, Publisher: The Royal Society of Chemistry, ISSN: 1460-4744. DOI: 10.1039/B919877F.

[20] X.-B. Cheng, R. Zhang, C.-Z. Zhao and Q. Zhang, 'Toward Safe Lithium Metal Anode in Rechargeable Batteries: A Review', eng, *Chemical Reviews*, vol. 117, no. 15, pp. 10 403–10 473, Aug. 2017, ISSN: 1520-6890. DOI: 10.1021/acs.chemrev.7b00115.

[21] D. Lin, Y. Liu and Y. Cui, 'Reviving the lithium metal anode for high-energy batteries', en, *Nature Nanotechnology*, vol. 12, no. 3, pp. 194–206, Mar. 2017, Number: 3 Publisher: Nature Publishing Group, ISSN: 1748-3395. DOI: 10.1038/nnano.2017.16.

[22] T. Tian, T.-W. Zhang, Y.-C. Yin *et al.*, 'Blow-Spinning Enabled Precise Doping and Coating for Improving High-Voltage Lithium Cobalt Oxide Cathode Performance', eng, *Nano Letters*, vol. 20, no. 1, pp. 677–685, Jan. 2020, ISSN: 1530-6992. DOI: 10.1021/acs.nanolett.9b04486.

[23] X. Wang, X. Wang and Y. Lu, 'Realizing High Voltage Lithium Cobalt Oxide in Lithium-Ion Batteries', en, *Industrial & Engineering Chemistry Research*, vol. 58, no. 24, pp. 10 119–10 139, Jun. 2019, ISSN: 0888-5885, 1520-5045. DOI: 10.1021/acs.iecr.9b01236.

[24] R. Jung, M. Metzger, F. Maglia, C. Stinner and H. A. Gasteiger, 'Oxygen Release and Its Effect on the Cycling Stability of LiNi $_x$ Mn $_y$ Co $_z$ O $_2$ (NMC) Cathode Materials for Li-Ion Batteries', en, *Journal of The Electrochemical Society*, vol. 164, no. 7, A1361–A1377, 2017, ISSN: 0013-4651, 1945-7111. DOI: 10.1149/2.0021707jes.

[25] J. Xia, L. Ma, K. J. Nelson, M. Nie, Z. Lu and J. R. Dahn, 'A Study of Li-Ion Cells Operated to 4.5 V and at 55°C', en, *Journal of The Electrochemical Society*, vol. 163, no. 10, A2399, Sep. 2016, Publisher: IOP Publishing, ISSN: 1945-7111. DOI: 10.1149/2.1211610jes.

[26] A. Purwanto, C. Satria Yudha, U. Ubaidillah, H. Widiyandari, T. Ogi and H. Haerudin, 'NCA cathode material: Synthesis methods and performance enhancement efforts', *Materials Research Express*, vol. 5, p. 122001, Dec. 2018, ADS Bibcode: 2018MRE.....5l2001P, ISSN: 2053-1591. DOI: 10.1088/2053-1591/aae167.

[27] J. He, H. Zhong, J. Wang and L. Zhang, 'Investigation on xanthan gum as novel water soluble binder for LiFePO4 cathode in lithium-ion batteries', en, *Journal of Alloys and Compounds*, vol. 714, pp. 409–418, Aug. 2017, ISSN: 0925-8388. DOI: 10.1016/j.jallcom.2017.04.238.

[28] T. Kozawa, T. Harata and M. Naito, 'Fabrication of an LiMn2O4@LiMnPO4 composite cathode for improved cycling performance at high temperatures', *Journal of Asian Ceramic Societies*, vol. 8, no. 2, pp. 309–317, Apr. 2020, Publisher: Taylor & Francis _eprint: https://doi.org/10.1080/21870764.2020.1743413, ISSN: null. DOI: 10.1080/21870764.2020.1743413.

[29] H. Xu, H. Zhang, J. Ma *et al.*, 'Overcoming the challenges of 5 V spinel LiNi0.5Mn1.5O4 cathodes with solid polymer electrolytes', *ACS Energy Letters*, vol. 2019, Oct. 2019. DOI: 10.1021/acsenergylett.9b01871.

[30] G. Ganas, G. Kastrinaki, D. Zarvalis *et al.*, 'Synthesis and characterization of LNMO cathode materials for lithium-ion batteries', en, *Materials Today: Proceedings*, 11th Panhellenic Scientific Conference on Chemical Engineering, 25-27 May 2017, vol. 5, no. 14, Part 1, pp. 27416–27424, Jan. 2018, ISSN: 2214-7853. DOI: 10.1016/j.matpr.2018.09.059.

[31] C. Tan, N. Wang, Q. Pan *et al.*, 'Enhancing the Electrochemical Performance of a High-Voltage LiNi0.5 Mn1.5 O4 Cathode in a Carbonate-Based Electrolyte with a Novel and Low-Cost Functional Additive', eng, *Chemistry (Weinheim an Der Bergstrasse, Germany)*, vol. 26, no. 53, pp. 12233–12241, Sep. 2020, ISSN: 1521-3765. DOI: 10.1002/chem.202001870.

[32] P. Zhu, D. Gastol, J. Marshall, R. Sommerville, V. Goodship and E. Kendrick, 'A review of current collectors for lithium-ion batteries', en, *Journal of Power Sources*, vol. 485, p. 229321, Feb. 2021, ISSN: 0378-7753. DOI: 10.1016/j.jpowsour.2020.229321.

[33] X. Zhang, X. Chang, Y. Shen and Y. Xiang, 'Electrochemical-electrical-thermal modeling of a pouch-type lithium ion battery: An application to optimize temperature distribution', en, *Journal of Energy Storage*, vol. 11, pp. 249–257, Jun. 2017, ISSN: 2352-152X. DOI: 10.1016/j.est.2017.03.008.

[34] M. K. Sundklakk, 'An investigation of lithium-ion battery degradation during shallow-, deep-, and combined cycles', eng, Accepted: 2019-11-06T15:03:53Z, M.S. thesis, NTNU, 2019. [Online]. Available: https://ntnuopen.ntnu.no/ntnu-xmlui/handle/11250/2627029.

[35] J. Li, Y. Zhang, R. Shang *et al.*, 'Recent advances in lithium-ion battery separators with reversible/irreversible thermal shutdown capability', en, *Energy Storage Materials*, vol. 43, pp. 143–157, Dec. 2021, ISSN: 2405-8297. DOI: 10.1016/j.ensm.2021.08.046.

[36] M. S. Wahl, L. Spitthoff, H. I. Muri, A. Jinasena, O. S. Burheim and J. J. Lamb, 'The Importance of Optical Fibres for Internal Temperature Sensing in Lithium-ion Batteries during Operation', en, *Energies*, vol. 14, no. 12, p. 3617, Jun. 2021, ISSN: 1996-1073. DOI: 10.3390/en14123617.

[37] A. Wang, S. Kadam, H. Li, S. Shi and Y. Qi, 'Review on modeling of the anode solid electrolyte interphase (SEI) for lithium-ion batteries', en, *npj Computational Materials*, vol. 4, no. 1, pp. 1–26, Mar. 2018, Number: 1 Publisher: Nature Publishing Group, ISSN: 2057-3960. DOI: 10.1038/s41524-018-0064-0.

[38] T. Waldmann, M. Wilka, M. Kasper, M. Fleischhammer and M. Wohlfahrt-Mehrens, 'Temperature dependent ageing mechanisms in Lithium-ion batteries – A Post-Mortem study', en, *Journal of Power Sources*, vol. 262, pp. 129–135, Sep. 2014, ISSN: 0378-7753. DOI: 10.1016/j.jpowsour.2014.03.112.

[39] D. Wieboldt, M. Hahn and I. Ruff, 'Techniques for Raman Analysis of Lithium-Ion Batteries', en, Special Issues-06-01-2015, vol. 30, no. 6, Jun. 2015, Publisher: MJH Life Sciences. [Online]. Available: https://www.spectroscopyonline.com/view/techniques-raman-analysis-lithium-ion-batteries.

[40] M. A. Hannan, M. M. Hoque, A. Hussain, Y. Yusof and P. J. Ker, 'State-of-the-Art and Energy Management System of Lithium-Ion Batteries in Electric Vehicle Applications: Issues and Recommendations', *IEEE Access*, vol. 6, pp. 19 362–19 378, Mar. 2018. DOI: 10.1109/ACCESS.2018.2817655.

[41] C. Julien, A. Mauger, A. Vijh and K. Zaghib, 'Lithium Batteries', en, in *Lithium Batteries: Science and Technology*, C. Julien, A. Mauger, A. Vijh and K. Zaghib, Eds., Cham: Springer International Publishing, 2016, pp. 29–68, ISBN: 978-3-319-19108-9. DOI: 10.1007/978-3-319-19108-9_2.

[42] QuantumScape, *Charge Rates for Next-Generation Batteries*, en-US, Nov. 2021. [Online]. Available: https://www.quantumscape.com/resources/blog/distinguishing-charge-rates-for-next-generation-batteries/.

[43] S. Nordang, 'Revolve NTNU - Electric Race car: Investigation of Characteristics, Cycle life and Safety Regarding Lithium-ion Battery Cells', eng, Accepted: 2017-05-02T14:00:35Z, M.S. thesis, NTNU, 2016. [Online]. Available: https://ntnuopen.ntnu.no/ntnu-xmlui/handle/11250/2441429.

[44] N. Phattharasupakun, P. Bunyanidhi, P. Chiochan, N. Chanlek and M. Sawangphruk, 'Effect of charging protocols on electrochemical performance and failure mechanism of commercial level Ni-rich NMC811 thick electrode', en, *Electrochemistry Communications*, vol. 139, p. 107 309, Jun. 2022, ISSN: 1388-2481. DOI: 10.1016/j.elecom.2022.107309.

[45] K. Jadav, 'Design a Residential PV Power System with Battery Energy Storage', *International Journal on Advances in Engineering Technology and Science*, vol. 1, Dec. 2015.

[46] S. Ma, M. Jiang, P. Tao *et al.*, 'Temperature effect and thermal impact in lithium-ion batteries: A review', en, *Progress in Natural Science: Materials International*, vol. 28, no. 6, pp. 653–666, Dec. 2018, ISSN: 1002-0071. DOI: 10.1016/j.pnsc.2018.11.002.

[47] F. Richter, P. J. S. Vie, S. Kjelstrup and O. S. Burheim, 'Measurements of ageing and thermal conductivity in a secondary NMC-hard carbon Li-ion battery and the impact on internal temperature profiles', en, *Electrochimica Acta*, vol. 250, pp. 228–237, Oct. 2017, ISSN: 0013-4686. DOI: 10.1016/j.electacta.2017.07.173.

[48] O. Shagouri, 'Testing Lithium-ion batteries thermal conductivity', eng, Accepted: 2021-09-21T16:01:33Z, Bachelor thesis, NTNU, 2021. [Online]. Available: https://ntnuopen.ntnu.no/ntnu-xmlui/handle/11250/2779952.

[49] P. J. Osswald, M. d. Rosario, J. Garche, A. Jossen and H. E. Hoster, 'Fast and Accurate Measurement of Entropy Profiles of Commercial Lithium-Ion Cells', en, *Electrochimica Acta*, International Conference on Electrochemical Energy Science and Technology (EEST2014), vol. 177, pp. 270–276, Sep. 2015, ISSN: 0013-4686. DOI: 10.1016/j.electacta.2015.01.191.

[50] O. S. Burheim, M. A. Onsrud, J. G. Pharoah, F. Vullum-Bruer and P. J. S. Vie, 'Thermal Conductivity, Heat Sources and Temperature Profiles of Li-Ion Batteries', en, *ECS Transactions*, vol. 58, no. 48, p. 145, Apr. 2014, Publisher: IOP Publishing, ISSN: 1938-5862. DOI: 10.1149/05848.0145ecst.

[51] D. K. Kinoshita, *Electrochemical Oxygen Technology*, en. John Wiley & Sons, Aug. 1992, Google-Books-ID: 2m22CvObj80C, ISBN: 978-0-471-57043-1.

[52] O. S. Burheim, 'Chapter 6 - Electrochemical Energy Storage', en, in *Engineering Energy Storage*, O. S. Burheim, Ed., Academic Press, Jan. 2017, pp. 75–110, ISBN: 978-0-12-814100-7. DOI: 10.1016/B978-0-12-814100-7.00006-7.

[53] F. Richter, S. Kjelstrup, P. J. S. Vie and O. S. Burheim, 'Thermal conductivity and internal temperature profiles of Li-ion secondary batteries', en, *Journal of Power Sources*, vol. 359, pp. 592–600, Aug. 2017, ISSN: 0378-7753. DOI: 10.1016/j.jpowsour.2017.05.045.

[54] A. F. Gunnarshaug, P. J. S. Vie and S. Kjelstrup, 'Review—Reversible Heat Effects in Cells Relevant for Lithium-Ion Batteries', en, *Journal of The Electrochemical Society*, vol. 168, no. 5, p. 050 522, May 2021, ISSN: 0013-4651, 1945-7111. DOI: 10.1149/1945-7111/abfd73.

[55] X. Zhang, Z. Li, L. Luo, Y. Fan and Z. Du, 'A review on thermal management of lithium-ion batteries for electric vehicles', en, *Energy*, vol. 238, p. 121 652, Jan. 2022, ISSN: 0360-5442. DOI: 10.1016/j.energy.2021.121652.

[56] T. L. Bergman, T. L. Bergman, F. P. Incropera, D. P. DeWitt and A. S. Lavine, *Fundamentals of Heat and Mass Transfer*, en. John Wiley & Sons, Apr. 2011, Google-Books-ID: vvyIoXEywMoC, ISBN: 978-0-470-50197-9.

[57] T. Waldmann, G. Bisle, B.-I. Hogg *et al.*, 'Influence of Cell Design on Temperatures and Temperature Gradients in Lithium-Ion Cells: An In Operando Study', en, *Journal of The Electrochemical Society*, vol. 162, no. 6, A921–A927, 2015, ISSN: 0013-4651, 1945-7111. DOI: 10.1149/2.0561506jes.

[58] A. Tomaszewska, Z. Chu, X. Feng *et al.*, 'Lithium-ion battery fast charging: A review', en, *eTransportation*, vol. 1, p. 100 011, Aug. 2019, ISSN: 2590-1168. DOI: 10.1016/j.etran.2019.100011.

[59] *Why Use An SEM in Battery Research? - Nanoscience Instruments*, en-US, Section: Blogs, Feb. 2023. [Online]. Available: https://www.nanoscience.com/why-use-an-sem-in-battery-research/.

[60] S. Xiong, 'A study of the factors that affect lithium ion battery degradation', eng, Accepted: 2020-05-27T14:29:29Z, Thesis, University of Missouri–Columbia, 2019. [Online]. Available: https://mospace.umsystem.edu/xmlui/handle/10355/73777.

[61] J. Vetter, P. Novák, M. R. Wagner *et al.*, 'Ageing mechanisms in lithium-ion batteries', en, *Journal of Power Sources*, vol. 147, no. 1, pp. 269–281, Sep. 2005, ISSN: 0378-7753. DOI: 10.1016/j.jpowsour.2005.01.006.

[62] J. S. Edge, S. O'Kane, R. Prosser *et al.*, 'Lithium ion battery degradation: What you need to know', en, *Physical Chemistry Chemical Physics*, vol. 23, no. 14, pp. 8200–8221, 2021, Publisher: Royal Society of Chemistry. DOI: 10.1039/D1CP00359C.

[63] C. R. Birkl, M. R. Roberts, E. McTurk, P. G. Bruce and D. A. Howey, 'Degradation diagnostics for lithium ion cells', en, *Journal of Power Sources*, vol. 341, pp. 373–386, Feb. 2017, ISSN: 0378-7753. DOI: 10.1016/j.jpowsour.2016.12.011.

[64] M. Oyarbide, M. Arrinda, D. Sánchez *et al.*, 'Capacity and Impedance Estimation by Analysing and Modeling in Real Time Incremental Capacity Curves', en, *Energies*, vol. 13, no. 18, p. 4855, Jan. 2020, Number: 18 Publisher: Multidisciplinary Digital Publishing Institute, ISSN: 1996-1073. DOI: 10.3390/en13184855.

[65] S. K. Heiskanen, J. Kim and B. L. Lucht, 'Generation and Evolution of the Solid Electrolyte Interphase of Lithium-Ion Batteries', en, *Joule*, vol. 3, no. 10, pp. 2322–2333, Oct. 2019, ISSN: 2542-4351. DOI: 10.1016/j.joule.2019.08.018.

[66] Bobby, *What is Lithium Plating?*, en-US, May 2014. [Online]. Available: https://www.upsbatterycenter.com/blog/lithium-plating/.

[67] J. S. Edge et al., 'Lithium ion battery degradation: What you need to know', Mar. 2021. [Online]. Available: https://doi.org/10.1039/D1CP00359C.

[68] Melasta, *Lithium Polymer (Li-Po) Battery SLPBB042126 (3.7V, 6550mAh 15C)*, 2020. [Online]. Available: https://www.melasta.com/cells/li-po-cells.html.

[69] A. Barai, K. Uddin, W. Widanage, A. McGordon and P. Jennings, 'A study of the influence of measurement timescale on internal resistance characterisation methodologies for lithium-ion cells', *Scientific Reports*, vol. 8, Jan. 2018. DOI: 10.1038/s41598-017-18424-5.

[70] W. Waag, S. Käbitz and D. U. Sauer, 'Experimental investigation of the lithium-ion battery impedance characteristic at various conditions and aging states and its influence on the application', en, *Applied Energy*, Special Issue on Advances in sustainable biofuel production and use - XIX International Symposium on Alcohol Fuels - ISAF, vol. 102, pp. 885–897, Feb. 2013, ISSN: 0306-2619. DOI: 10.1016/j.apenergy.2012.09.030.

[71] T. Kalogiannis, D. I. Stroe, J. Nyborg, K. Nørregaard, A. E. Christensen and E. Schaltz, 'Incremental Capacity Analysis of a Lithium-Ion Battery Pack for Different Charging Rates', en, *ECS Transactions*, vol. 77, no. 11, p. 403, Jul. 2017, Publisher: IOP Publishing, ISSN: 1938-5862. DOI: 10.1149/07711.0403ecst.

[72] K. Honkura and T. Horiba, 'Study of the deterioration mechanism of Li-CoO2/graphite cells in charge/discharge cycles using the discharge curve analysis', en, *Journal of Power Sources*, vol. 264, pp. 140–146, Oct. 2014, ISSN: 0378-7753. DOI: 10.1016/j.jpowsour.2014.04.036.

[73] A. Hales et al., 'The Surface Cell Cooling Coefficient: A Standard to Define Heat Rejection from Lithium Ion Battery Pouch Cells', Jan. 2020. [Online]. Available: http://dx.doi.org/10.1149/1945-7111/ab6985.

[74] O. Burheim, P. J. S. Vie, J. G. Pharoah and S. Kjelstrup, 'Ex situ measurements of through-plane thermal conductivities in a polymer electrolyte fuel cell', en, *Journal of Power Sources*, vol. 195, no. 1, pp. 249–256, Jan. 2010, ISSN: 0378-7753. DOI: 10.1016/j.jpowsour.2009.06.077.

[75] R. Siburian, H. Sihotang, S. Raja, M. Supeno and C. Simanjuntak, 'New Route to Synthesize of Graphene Nano Sheets', *Oriental Journal of Chemistry*, vol. 34, pp. 182–187, Feb. 2018. DOI: 10.13005/ojc/340120.

Appendix

A   Melasta SLPBB042126

Data sheet of the Melasta Cell with cell specifications.

Lithium Polymer (Li-Po) Battery
## SLPBB042126 (3.7V, 6550mAh 15C)

melasta®

Features of Lithium-Polymer Battery

- **Longer Cycle Life:** Offers up to 20 times longer cycle life and five times longer float/calendar life than lead acid battery, helping to minimize replacement cost and reduce total cost of ownership.

- **Lighter Weight:** About 40% of the weight of a comparable lead acid battery. A 'drop in' replacement for lead acid batteries.

- **Higher Power**: Delivers twice power of lead acid battery, even high discharge rate, while maintaining high energy capacity.

- **Wider Temperature Range:** -20 C~60 C.

- **Superior Safety:** Lithium Polymer chemistry eliminates the risk of explosion or combustion due to high impact, overcharging or short circuit situation.

- **Increased Flexibility:** Modular design enables deployment with several batteries both in series and in parallel.
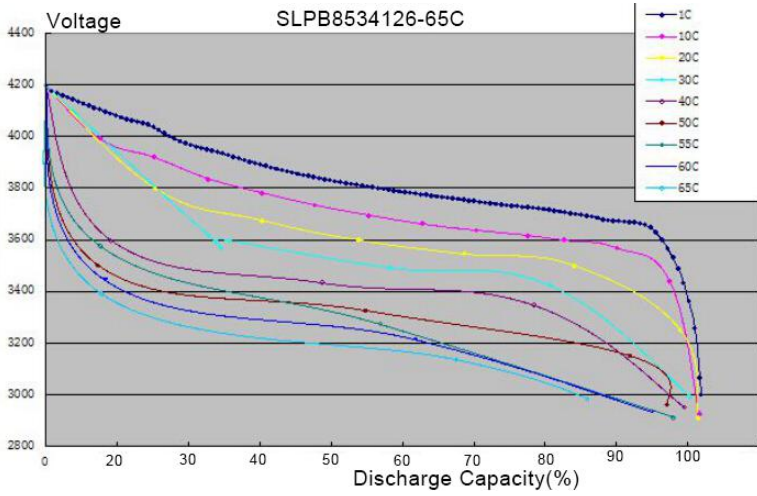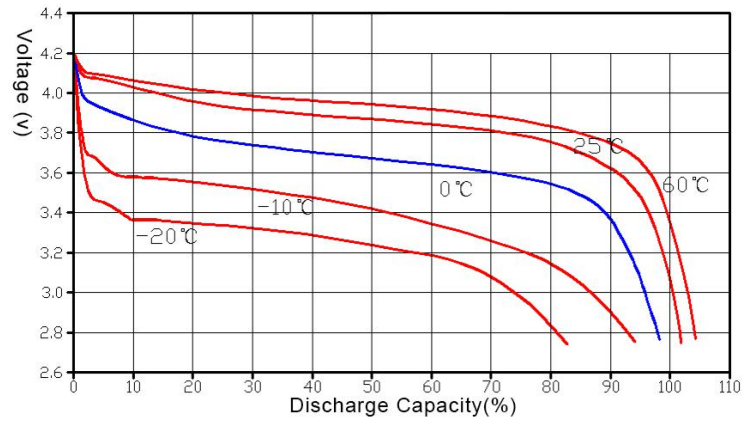
SGS

- **MSDS**
- **UN38.3**
- **CE**
- **FCC**

Physical Dimension
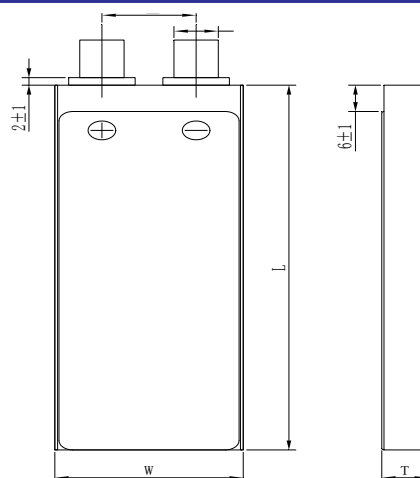
Specification

Electrical Characteristics	Nominal Voltage	3.7V
	Nominal Capacity	6550mAh
	Energy	24.235Wh
	Internal Resistance	≤1.5mΩ
	Cycle Life	>100 cycles @Charge:0.5C,Discharge:15C 80%DOD
	Months Self Discharge	<3%
	Efficiency of Charge	100% @0.5C
	Efficiency of Discharge	96~99% @1.0C
Standard Charge	Charge Voltage	4.2V
	Charge Mode	0.2C to 4.2V, then 4.2V,charge current to $0.02C_5A$ (CC/CV)
	Charger Current	1.31A
	Max. Charge Current	$2.0C_5A$
	Charge Cut-off Voltage	4.2±0.03V
Standard Discharge	Continuous Current	1.31A
	Max.Discharge Current	$15C_5A$
	Discharge Cut-off Voltage	3.0V
Environmental	Charge Temperature	0℃ to 45℃ @60±25% Relative Humidity
	Discharge Temperature	-20℃ to 60℃ @60±25% Relative Humidity
	Storage Temperature	0℃ to 40℃ @60±25% Relative Humidity
	Water Dust Resistance	/
Mechanical	Dimensions (mm.)	L127.0±0.5*W42.0±0.58*T10.2±0.3mm
	Distance between 2 tabs	21±1mm
	Weight (g.)	Approx:126.0±3.0g

Lithium Polymer (Li-Po) Battery
SLPBB042126 (3.7V, 6550mAh 15C)

Different Rate Discharge Curve

SLPB8534126-65C

Legend: 1C, 10C, 20C, 30C, 40C, 50C, 55C, 60C, 65C

Different Temperature Discharge Curve

Different Rate Charge Curve